

**EXTENSION OF MOIRE INTERFEROMETRY INTO  
THE ULTRA-HIGH SENSITIVITY DOMAIN**

by

Bongtae Han

Dissertation submitted to the Faculty of the  
Virginia Polytechnic Institute and State University  
in partial fulfillment of the requirements for the degree of

**DOCTOR OF PHILOSOPHY**

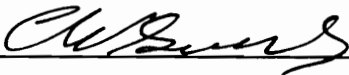
in

Engineering Mechanics

APPROVED:



D. Post, Chairman



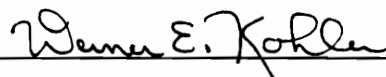
C. W. Smith



N. E. Dowling



D. A. Dillard



W. Kohler

March 1991

Blacksburg, VA 24061

# **EXTENSION OF MOIRE INTERFEROMETRY INTO THE ULTRA-HIGH SENSITIVITY DOMAIN**

by

Bongtae Han

Committee Chairman: Daniel Post

Engineering Mechanics

(ABSTRACT)

The objective of this research was to provide means for the experimental analysis of deformations encountered in micromechanics. Whole field contour maps of U and V displacements in a microscopic field of view were desired. Since displacements within a small field can be very small even when strains are large, ultra-high sensitivity is required. The specific objective was displacement sensitivity of 50 nm per fringe contour, which corresponds to that of moire with 20,000 lines per mm, in combination with spatial resolution of the optical microscope (2-5  $\mu\text{m}$ ).

The objective was achieved by the following developments. First, the basic sensitivity of moire interferometry was increased beyond the previously conceived theoretical limit. This was accomplished by creating the virtual reference grating inside a refractive medium instead of air, thus shortening the wavelength of light. A very compact four beam moire interferometer in a refractive medium was developed for microscopic viewing, which produced a basic sensitivity of 208 nm per fringe order. Its configuration made it inherently

stable and relatively insensitive to environmental disturbances. An optical microscope was employed as the image recording system to obtain the desired spatial resolution.

Secondly, a fringe multiplication scheme was implemented. Here, an automatic fringe shifting and fringe sharpening scheme was developed, wherein very thin fringe contours of order  $N^* = \beta N$  were produced, where  $N$  is the fringe order in the basic moire pattern and  $\beta$  is a fringe multiplication factor. A factor of 12 was achieved, providing a sensitivity of 17 nm per fringe contour. This corresponds to moire with 57,600 lines per mm (1,463,000 lines per in.), which exceeds the sensitivity objective. The mechanical and electronic systems implemented here are remarkably robust and quick.

The method was demonstrated with three practical applications: interface strains in a thick  $0^\circ/90^\circ$  graphite/epoxy composite, fiber/matrix deformations of metal/matrix composites, and thermal deformation around a solder joint in a microelectronic subassembly.

## ACKNOWLEDGEMENTS

The author would like to express his sincere gratitude to Prof. Dan Post, who as advisor and committee chairman, offered his unselfish concern, support, and advise in personal as well as professional matters. The constant spiritual support and the help for a long period from Prof. Daniel Post and his wife Frieda Post was indispensable in completing this work and is gratefully acknowledged.

Special appreciation and love is extended to the author's wife, Sunny, for consistent encouragement, understanding, patience and love throughout his graduate career; the author's son, Dongsoo for spiritually strengthening the author; and his parents and parents-in-law for inspiration and support.

In addition, the author wishes to acknowledge and thank:

- The National Science Foundation (Grant No. MSS-8913942), Dr. Rembert Jones, Technical Officer, the Office of Naval Research (Grant No. N00014-90-J1688), and the Virginia Center for Innovative Technology (Grant No. MAT-90-010) for sponsoring this work.
- his committee members, C. W. Smith, N. E. Dowling, D. A. Dillard, and W. Kohler for their participation and guidance.
- his colleagues in the photomechanics group, Peter Ifju, Ray Boeman, Yifan Guo, and Judy Wood whose help, cooperation and most importantly friendship over the years, is greatly appreciated. Peter's help with figures is especially appreciated.

- Dr. Harry Morimoto for helping the author to have the basic understanding of image processing.
- Dr. Steve Johnson of NASA-Langley Research Center for providing silicon-carbide/aluminum specimen.
- Dr. Mike Hyer of VPI & SU for providing boron/aluminum specimen.
- Dr. Yifan Guo of IBM, Endicott, NY for providing microelectronic subassembly.
- the machine shop personnel, Bob Davis, Archie Montgomery and Bill Shaver, for their expert machining of many fixtures and specimens over the years.
- Paula Lee for her consistent help in preparation of this dissertation.
- Joosik Lee, Shih-Yung Lin, and Jau-Je Wu for their continued friendship and spirit of cooperation.

# TABLE OF CONTENTS

ABSTRACT .....	ii
ACKNOWLEDGEMENTS.....	iv
LIST OF TABLES.....	viii
LIST OF FIGURES.....	ix
1.0 INTRODUCTION.....	1
1.1 Motivation and Literature Review.....	1
1.2 Background - Moire Interferometry .....	4
1.2.1 Basic Principle.....	4
1.2.2 Theoretical Limit of Sensitivity.....	7
1.3 Objective .....	8
1.4 Two-step Process.....	9
1.5 Interpretation of Fringe Formation in Moire Interferometry.....	11
2.0 MOIRE INTERFEROMETRY IN A REFRACTIVE MEDIUM.....	15
2.1 Introduction.....	15
2.2 Wavelength of Light in a Refractive Medium.....	15
2.3 Sensitivity of Moire Interferometry in Refractive Medium.....	16
2.4 Optical Configurations.....	20
2.4.1 Configuration 1.....	20
2.4.2 Configuration 2.....	25
2.4.3 Configuration 3.....	27
3.0 MICROSCOPIC MOIRE INTERFEROMETRY.....	30
3.1 Introduction.....	30
3.2 Enhancement of Sensitivity.....	30

3.3 Immersion Interferometer.....	32
4.0 FRINGE SHIFTING.....	36
4.1 Introduction.....	36
4.2 Fringe Shifting .....	36
4.3 Fringe Shifting Scheme.....	39
4.4 Translation and Calibration.....	43
5.0 MECHANICAL CONFIGURATION OF THE APPARATUS.....	48
6.0 FRINGE SHARPENING AND MULTIPLICATION .....	50
6.1 Introduction.....	50
6.2 Scheme 1 .....	53
6.3 Scheme 2 .....	60
6.4 Combination of Fringe-shifted Patterns .....	65
7.0 DEMONSTRATIONS.....	68
7.1 Normal Strains across an Interface in a Thick Graphite/Epoxy Composite.....	68
7.2 Deformation of Metal/Matrix Composites.....	75
7.3 Thermal Deformation of a Microelectronic Assembly.....	79
8.0 DISCUSSION AND FUTURE WORK .....	88
8.1 Further Enhancement of the Sensitivity of Moire Interferometry .....	88
8.2 Specimen Grating.....	89
9.0 CONCLUSIONS.....	91
10.0 REFERENCES .....	92
Vita.....	99

## LIST OF TABLES

Table 1. Theoretical limits for various optical glasses. ....	18
Table 2. Theoretical limits for an optical crystal. ....	18
Table 3. Practical limits of sensitivity. ....	19
Table 4. Phase values and fringe orders for an example of scheme 2. ....	63



## LIST OF FIGURES

Fig. 1 Schematic diagrams of optical arrangement for moire interferometry.....	5
Fig. 2 Intensity distribution for the original and transformed field of fringes, where $\beta$ is 6. ....	10
Fig. 3 Moire interferometry. Warped wavefronts A" and B" emerge from the deformed specimen grating and interfere to form the moire pattern.....	12
Fig. 4 (a) Configuration 1 and (b) its variation.....	21
Fig. 5 Illustrations for (a) law of refraction, (b) rays creating a ghost pattern and (c) a solution to eliminate the ghost pattern. ....	24
Fig. 6 Configuration 2.....	26
Fig. 7 (a) Configuration 3 and (b) illustration of compensation for chromatic light. ....	28
Fig. 8 Frequency of virtual reference grating (a) in air and (b) in BK7.....	31
Fig. 9 Four-beam immersion interferometer. ....	33
Fig. 10 Fabrication of the main element of the immersion interferometer. ....	34
Fig. 11 Illustration of fringe shifting in geometrical moire. (a) an original pattern (b) a shifted pattern where the reference grating is translated horizontally by half of its pitch.....	37
Fig. 12 Schematic diagram of fringe shifting scheme.....	40
Fig. 13 Physical explanation of shifting scheme.....	41
Fig. 14 The translation device.....	44

Fig. 15	A block diagram of apparatus for calibration.....	45
Fig. 16	A flow chart for the calibration and fringe shifting process. ....	47
Fig. 17	The optical and mechanical assembly.....	49
Fig. 18	Illustration of intensity distributions of moire patterns and the corresponding binary images.....	51
Fig. 19	Illustration of scheme 1 for an idealized case.....	54
Fig. 20	Illustration of scheme 1 on a whole field base.....	56
Fig. 21	Illustration of scheme 1 for the case of nonuniform illumination with optical noise. ....	59
Fig. 22	Illustration of scheme 2 for the case of nonuniform illumination.....	64
Fig. 23	A flow chart for obtaining the composite contour map.....	67
Fig. 24	The graphite/epoxy composite specimen.....	69
Fig. 25	$N_y^*$ field near 0/90° interfaces. Sensitivity is 104nm per fringe contour.....	70
Fig. 26	$N_y^*$ field with carrier fringes of rotation. Sensitivity is 104nm per fringe contour.....	71
Fig. 27	$N_y^*$ field with carrier fringes of rotation and extension. Sensitivity is 26nm per fringe contour. ....	73
Fig. 28	$N_y^*$ field with carrier fringes of rotation and extension, documented in a different location. Sensitivity is 26nm per fringe contour.....	74
Fig. 29	Strain distribution across the interface.....	76
Fig. 30	The metal/matrix specimens.....	77

Fig. 31 $N_y^*$ field of the boron/aluminum specimen. Sensitivity is 26nm per fringe contour.....	78
Fig. 32 $N_y^*$ field of the silicon-carbide/aluminum specimen. Sensitivity is 52nm per fringe contour. ....	80
Fig. 33 $N_x^*$ field of the silicon-carbide/aluminum specimen. Sensitivity is 52nm per fringe contour. ....	81
Fig. 34 $N_y^*$ field of the silicon-carbide/aluminum specimen with carrier fringes of extension for a higher load. Sensitivity is 52nm per fringe contour.....	82
Fig. 35 Illustration of the solder ball interconnection technique.....	83
Fig. 36 $N_y^*$ field around a solder joint. Sensitivity is 17nm per fringe contour.....	86
Fig. 37 $N_x^*$ field around a solder joint. Sensitivity is 17nm per fringe contour.....	87

## **1.0 INTRODUCTION**

### **1.1 Motivation and Literature Review**

This research is intended to provide enhanced capabilities for experimental micromechanics analyses. In recent years, a considerable amount of study has been conducted to document micromechanical behavior of various solid materials [1-12]. This includes problems involving material discontinuities that exist near interfaces between grain boundaries in metals and ceramics, between fiber and matrix, and between laminae in fiber reinforced composites and geometrical discontinuities at cracks and sharp notches. These problems require an understanding of macro- and micro-material behavior, and thus they require experimental techniques that provide high sensitivity deformation measurements with large dynamic ranges. Among the many experimental techniques available today, moire interferometry stands as the most attractive approach since it is a strictly geometric method and it measures whole-field phenomenon.

The optical method called moire interferometry was developed largely in this decade [13-16]. Although it emerged quickly, the method has been improved in an evolutionary process. Moire interferometry retains the virtues of the traditional geometric moire method [17] but it extends the sensitivity of moire methods into the subwavelength range; moire interferometry with a sensitivity of  $0.417 \mu\text{m}$  ( $16.4 \mu\text{in.}$ ) per fringe order is practiced routinely in the VPI & SU Photomechanics Laboratory. In addition to the high sensitivity, other

remarkable features of this method such as whole-field measurement, excellent fringe contrast, high spatial resolution and extensive dynamic range make it suitable for the solutions of various practical problems [18-27].

In micromechanics, many studies require microscopic viewing of small zones of the specimen. Since displacement is strain multiplied by distance, the relative displacements within a small field can be very small, even when the strains are not small. Accordingly very high sensitivity that is considerably higher than  $0.417 \mu\text{m}$  per fringe order is needed to map those displacement fields.

During the past few decades, many researchers have attempted to increase the sensitivity of moire methods. These attempts have been made by two different approaches: optical filtering techniques and digital image processing.

In the case of optical filtering techniques, distorted gratings that carry the displacement information are produced either by using carrier pattern techniques [28] or by photographing deformed specimen gratings. Then, the distorted gratings are interrogated by moire fringe multiplication to extract the whole-field displacement information with enhanced sensitivity. Various concepts of moire fringe multiplication were developed separately by Post [29-31] and Sciammarella [32]. Basically, the technique involves superposition of a reference grating, which may be either real or virtual, with a deformed grating and filtering the transmitted light to form a moire pattern by interference of selected diffraction beams. Such methods were used by Post and MacLaughlin [33] and later by Sanford and Graham [34]. Morimoto [35] and later Czarnek

[36] demonstrated methods with higher sensitivity utilizing optical filtering. In each of these cases, the resulting interference pattern showed substantial optical noise. In addition, the above work was conducted at lower sensitivities than that accomplished here.

As digital image processing has become easily accessible to the experimentalist, many image processing techniques have been developed to increase the sensitivity of moire interferometry. Hunter et al. [37,38] proposed a method to obtain a continuous displacement field in which a fast fourier transform technique was utilized to filter out high frequency noise and to describe a displacement field as a continuous function. Voloshin et al. [39] used the variations of light intensity of a moire pattern to determine fractional fringe orders. Hung et al. [40] also used a fast fourier transform technique but they increased the sensitivity by choosing a particular harmonic component in the transformed domain. Yu [41] increased the sensitivity by manipulating digital images by use of a trigonometric relationship. In all cases, the intensity distribution was assumed to be a certain functional form and the function was manipulated by a computer. Although high frequency noise could be eliminated by various filtering algorithms, those techniques could not avoid distortion of intensity distributions caused by low frequency noise such as nonuniform illumination and nonuniform quality of the specimen grating. The distortion of the intensity distribution could yield significant errors in determining displacement fields, especially for those problems encountered in micromechanics which have localized regions with high strain gradients.

Although all the optical filtering and image processing techniques described above were proposed to increase the sensitivity of displacement measurements, very few practical applications to macro- or micromechanical problems were found in the literature. This would be due to their inherent shortcomings such as optical noise, limited dynamic range of measurements, and insufficient sensitivity and accuracy.

## **1.2 Background - Moire Interferometry**

### **1.2.1 Basic Principle**

Moire interferometry [42] provides whole-field in-plane displacement fields,  $U$  and  $V$ . It is an optical method using coherent light and featuring subwavelength sensitivity and high spatial resolution. The method is similar in many ways to traditional geometric moire methods, but its sensitivity is greater by almost two orders of magnitude.

The basic principle is depicted schematically in Fig. 1. In this method, a crossed-line diffraction grating is replicated on a specimen and it deforms together with the loaded specimen. Two beams of coherent light  $A$ ,  $B$  illuminate the specimen grating obliquely from angles  $+\alpha$  and  $-\alpha$ , which create walls of constructive and destructive interference in the zone of their intersection. This interference is cut by the plane of the specimen surface, where an array of parallel and very closely spaced fringes are formed. These fringes are essentially bright and dark bars and they act like the reference grating of

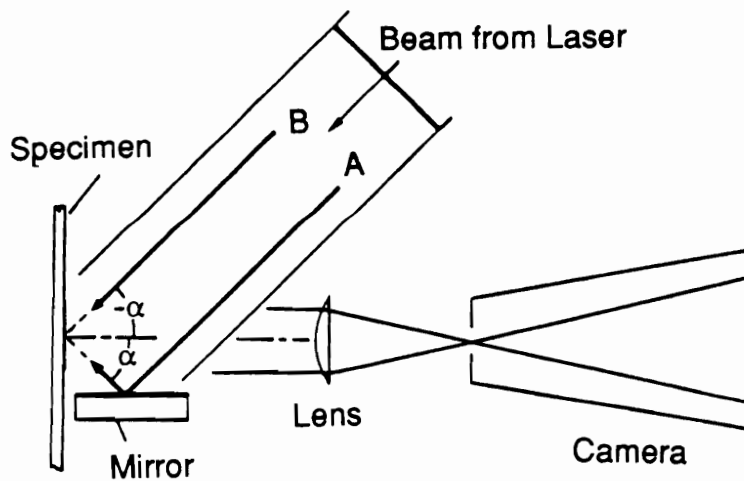
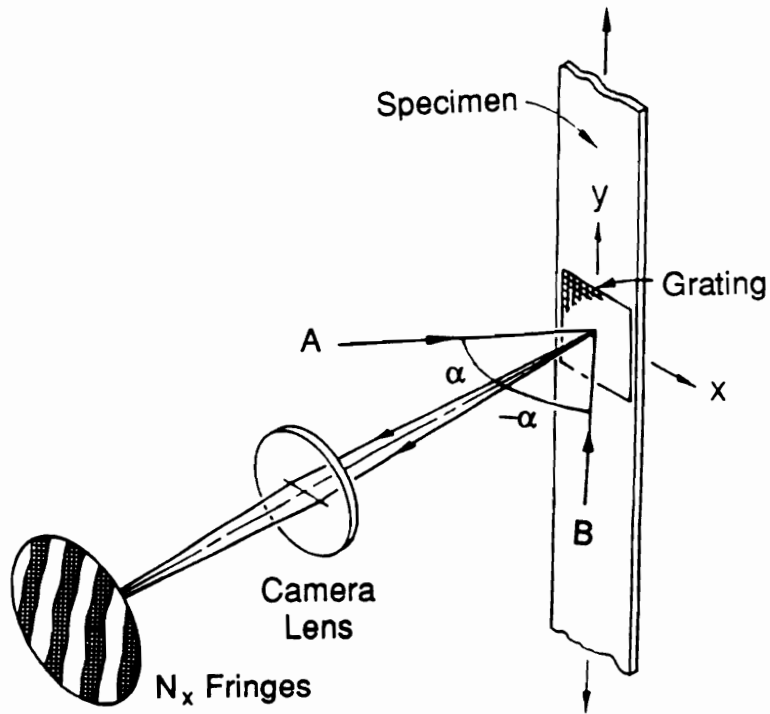


Fig. 1 Schematic diagrams of optical arrangement for moiré interferometry.



geometric moire. This array of fringes is called a virtual reference grating. The frequency,  $f$ , of the virtual reference grating is determined by

$$f = \frac{2}{\lambda} \sin\alpha \quad (1)$$

where  $\lambda$  is the wavelength of light employed and  $\alpha$  is the angle of incidence (Fig. 1).

The specimen grating and virtual reference grating interact to form a moire pattern which is a contour map of  $N_x$  or the in-plane specimen displacement  $U$ . Additional input beams C and D in the vertical plane (not shown) produce the moire pattern for the  $N_y$  field. The patterns are photographed with a camera focused on the specimen surface. Then, in-plane displacement components are determined by

$$U = \frac{1}{f} N_x, \quad V = \frac{1}{f} N_y \quad (2)$$

where  $N$  is the fringe order at each point in the moire pattern. When the displacement fields are established, the strain components can be calculated from the displacement derivatives by

$$\epsilon_x = \frac{\partial U}{\partial x} = \frac{1}{f} \frac{\partial N_x}{\partial x} \quad \epsilon_y = \frac{\partial V}{\partial y} = \frac{1}{f} \frac{\partial N_y}{\partial y} \quad (3)$$

$$\gamma_{xy} = \frac{\partial U}{\partial y} + \frac{\partial V}{\partial x} = \frac{1}{f} \left( \frac{\partial N_x}{\partial y} + \frac{\partial N_y}{\partial x} \right) \quad (4)$$

where  $\epsilon_x$ ,  $\epsilon_y$  are normal strain components and  $\gamma_{xy}$  is engineering shear strain component, respectively.

The lower part of Fig. 1 illustrates a suitable optical arrangement in which a parallel beam of laser light arrives at the specimen with angle  $-\alpha$ , while a portion of the same beam is redirected by a plane mirror to arrive with the symmetrical angle  $\alpha$ .

### 1.2.2 Theoretical Limit of Sensitivity

This research is based on moire interferometry. Equation (2) defines its sensitivity as  $1/f$  displacement per fringe order. Since higher sensitivity corresponds to a smaller displacement per fringe order, it is clear from Eq. (1) that shorter wavelengths are desired for higher sensitivities. Then, for a fixed  $\lambda$ , the sensitivity approaches its theoretical limit as angle  $\alpha$  approaches  $90^\circ$ . In the limit, the maximum sensitivity is  $\lambda/2$  per fringe order.

When  $\alpha = 64^\circ$ ,  $\sin\alpha$  is already 90% of its maximum value and there is not much to be gained by using larger angles. However, an experiment conducted at 97.6% of the theoretical limit verified that moire interferometry is effective even near its theoretical limit [43]. For visible light of low-blue wavelengths,  $f$  is limited to slightly more than 4000 lines per mm, corresponding to a sensitivity limit near 250nm displacement per fringe order.

### 1.3 Objective

The objective of the research is to develop an ultra-high sensitivity whole-field in-plane displacement measurement technique for micromechanics (the study of the mechanics of solids on a microscopic level). The sensitivity objective is 50 nm per fringe contour or better, which corresponds to that of moire with 20,000 lines per mm (500,000 lines per in.) or more.

The objective includes development of a new configuration of moire interferometry to maximize the basic sensitivity and stability, and development of a two-step process to achieve the sensitivity objective.

The objective also includes high spatial resolution (resolution of 2-5  $\mu\text{m}$ ), the maximization of signal-to-noise ratio and large dynamic range in deformation measurements (up to 10% strain).

The optical microscope with visible light is to be used. This avoids the severe limitations on the specimen size, the loading and the environmental conditions otherwise entailed by use of short (invisible) wavelength techniques such as electron microscopy, X-ray and neutron interferometry [44].

## 1.4 Two-step Process

A two-step process of moire interferometry is to be developed to achieve the sensitivity objective. It is expressed in Fig. 2. Whereas the whole-field fringe pattern of moire interferometry follows the intensity vs. fringe order relationship of curve N (step 1), a two-step process is to transform the distribution to that of curve N\* (step 2). The pattern representing the displacement field would exhibit  $\beta$  times as many fringe contours, where  $\beta$  is called the fringe multiplication factor. The contour interval would be reduced by a factor of  $\beta$ , and the sensitivity to displacements would be increased by the same factor. The resultant pattern would then represent specimen displacements by

$$U = \frac{N_x^*}{\beta f}, \quad V = \frac{N_y^*}{\beta f} \quad (5)$$

where  $N^*$  is the fringe order in the final pattern. As in all moire analysis for deformation studies, rigid-body displacements are inconsequential and the location of a point of  $N^* = 0$  is arbitrary. The relationship to the basic moire pattern is  $N^* = \beta N + k$ , where  $k$  is a constant for the whole field.

In this work, moire interferometry is used for step 1 to map an original displacement field. For step 2, fringe shifting and fringe sharpening are employed to record a sequence of shifted fringe contours, each shifted by a constant increment. Then the density of the final pattern is increased by combining the series of shifted fringe contours into a single contour map.

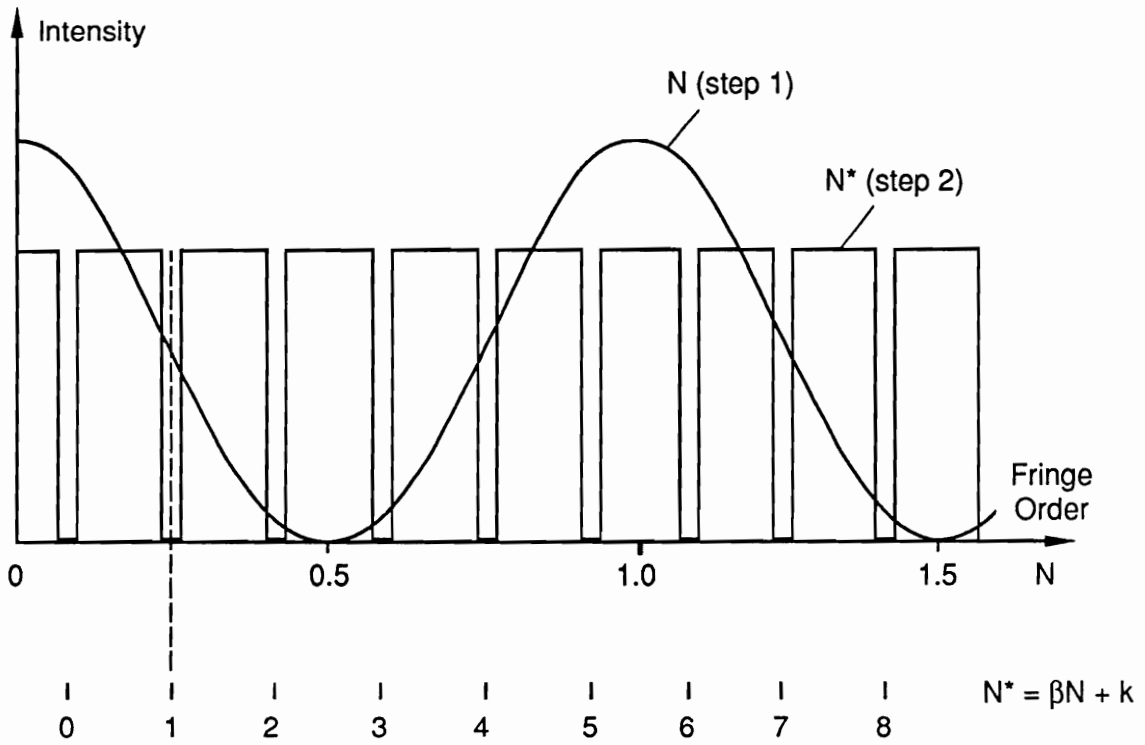


Fig. 2 Intensity distribution for the original and transformed field of fringes, where  $\beta$  is 6.

## 1.5 Interpretation of Fringe Formation in Moire Interferometry

The basic principle of moire interferometry was explained with the concept of a virtual reference grating. Although it is not a rigorous explanation of moire interferometry, it leads to easy understanding of the method. However, the existence of a reference grating is not an essential condition for the resulting interference fringes. In order to provide a firm background for the fringe-shifting process employed in this study, a more rigorous interpretation of fringe formation in moire interferometry is given from diffraction theory and wavefront interference theory [42, 45].

When a grating is illuminated by a collimated beam of light, diffracted beams will be governed by the well-known diffraction equation

$$\sin\theta_m = m\lambda f_s + \sin\alpha \quad (6)$$

where  $\theta_m$  is the diffraction angle of the  $m^{\text{th}}$  diffraction order,  $\lambda$  is the wavelength of light employed,  $f_s$  is the frequency of the grating and  $\alpha$  is the angle of incidence.

In moire interferometry, a high frequency phase-type grating is formed on the specimen and it deforms together with the specimen. In the method, two incident beams are symmetric with respect to the normal to the specimen grating as illustrated in Fig. 3. When the incident angles  $\alpha$  of the collimated beams satisfy the relationship

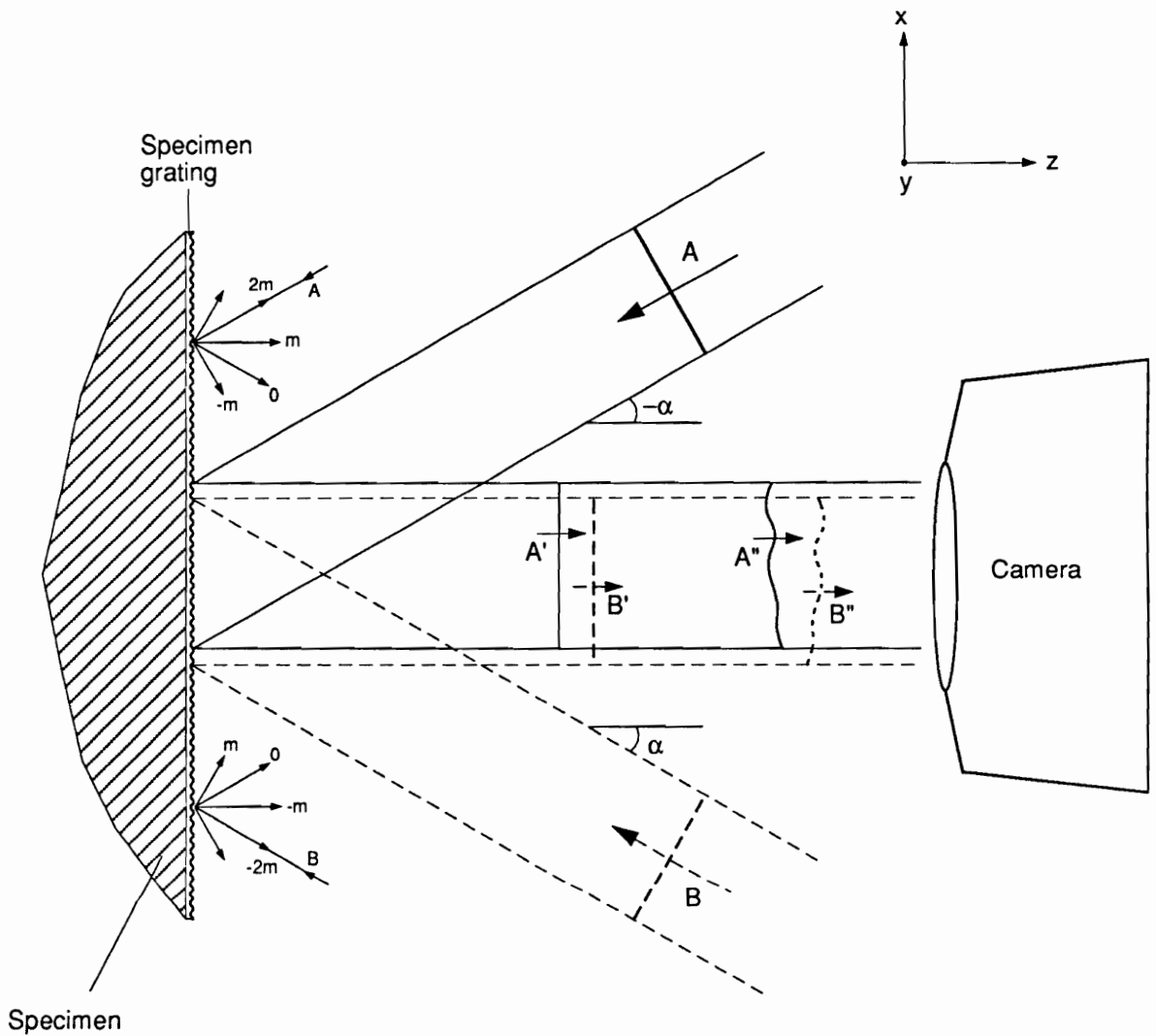


Fig. 3 Moiré interferometry. Warped wavefronts  $A''$  and  $B''$  emerge from the deformed specimen grating and interfere to form the moiré pattern.

$$\sin\alpha = m\lambda f_s = \frac{\lambda f}{2} \quad (7)$$

the  $+m^{\text{th}}$  and  $-m^{\text{th}}$  diffraction order of the incident beams A and B (Fig. 3), respectively, emerge along the normal to the specimen; here  $f$  is  $2mf_s$  where  $f_s$  is the frequency of the undeformed specimen grating. When the specimen grating is not deformed, the two diffracted beams A', B' have plane and parallel wavefronts and their mutual interference produces a uniform intensity throughout the field; this is called a null field, a field devoid of fringes.

When the specimen deforms, the wavefronts become warped (A'', B'' in Fig. 3) and interfere with each other to produce fringe patterns. Then, a displacement can be described by [45]

$$U(x,y) = \frac{1}{2mf_s} \left( N(x,y) - \frac{\delta}{\lambda} \right) = \frac{1}{f} \left( N(x,y) - \frac{\delta}{\lambda} \right) \quad (8)$$

where  $U(x,y)$  is a displacement component in the  $x$ -direction (essentially perpendicular to the specimen grating lines),  $N(x,y)$  is the fringe order and  $\delta$  is the difference between optical path lengths traveled by the two rays through specimen point  $x, y$  (rays from beams A and B in Fig. 3) from a common light source to the camera image plane.

Equation (8) is identical to Eq. (2) except for the constant  $\delta/\lambda$ . The constant is equivalent to a uniform displacement throughout the field, or a rigid-body translation. Although we are not interested in rigid-body motions



when studying deformations, the existence of the constant provides a useful flexibility which will be discussed later. It is interesting to note, too, that the sensitivity depends on  $2m$  times the frequency of the specimen grating. In normal practice of moire interferometry,  $m$  is equal to 1. The dependency of sensitivity on  $m$  and the frequency of the specimen grating will be discussed later, too.

## 2.0 MOIRE INTERFEROMETRY IN A REFRACTIVE MEDIUM

### 2.1 Introduction

By combining Eq. (1) and (2),

$$U(x,y) = \frac{\lambda}{2\sin\alpha} N_x \quad (9)$$

Since the sensitivity of moire interferometry increases as the displacement per fringe order decreases, the sensitivity is increased as the wavelength of light  $\lambda$  is decreased or the angle of incidence  $\alpha$  is increased. But, as mentioned earlier, there is not much to be gained by using incident angles larger than  $64^\circ$ . The remaining variable is the wavelength of light. One can manipulate visible light to decrease its wavelength without changing its color or visibility.

In this chapter, it will be discussed in detail how the wavelength of light can be reduced in a refractive medium, and thus how much the basic sensitivity of moire interferometry can be increased. Various optical configurations of moire interferometry for operation in a refractive medium will be also introduced.

### 2.2 Wavelength of Light in a Refractive Medium

The velocity,  $C$ , of light in vacuum [46] is known to be

$$C = v\lambda \quad (10)$$

where  $C$  is a universal constant for all electromagnetic radiation and  $v, \lambda$  is the frequency and wavelength, respectively, of the radiating wavetrain. The velocity of light in a refractive medium is decreased according to the relationship

$$V_m = \frac{C}{n} = \frac{v\lambda}{n} \quad (11)$$

where  $V_m$  is the velocity and  $n$  is the refractive index of the medium.

For any wavetrain in the electromagnetic spectrum, the frequency is the same in all media [46], and therefore the wavelength is decreased by the same ratio as the velocity, that is,

$$\lambda_m = \frac{\lambda}{n} \quad (12)$$

where  $\lambda_m$  is the wavelength of light in the refractive medium.

### **2.3 Sensitivity of Moire Interferometry in Refractive Medium**

From Eqs. (1) and (11), the frequency,  $f_m$ , of a virtual reference grating in a refractive medium can be expressed as

$$f_m = \frac{2\sin \alpha}{\lambda_m} = \frac{2n\sin \alpha}{\lambda} \quad (13)$$

It is clear from Eq. (13) that, for a given light source of wavelength  $\lambda$  in vacuum, the frequency of the virtual reference grating in a refractive medium is increased by a factor of  $n$  and the theoretical limit of the sensitivity is also increased by the same factor.

For example, the wavelength of green argon laser light is 514 nm in air, but it is reduced to 343nm in glass of refractive index 1.5. Thus, the maximum frequency of the virtual reference grating is increased from 3890 lines/mm (in air) to 5840 lines/mm (in glass), which corresponds to the sensitivity of 170 nm per fringe order.

Table 1 lists various optical glasses and their refractive indices. It also shows the theoretical upper limits for virtual reference grating frequencies and the corresponding limits of sensitivity when green laser light ( $\lambda = 514\text{nm}$ ) is employed. Since the maximum frequency of a virtual reference grating is directly proportional to the refractive index, it can be increased by up to 1.98 with respect to that in air. The maximum frequency of virtual reference gratings can be increased even more by using optical crystals. If Rutile ( $\text{TiO}_2$ ) is used with the plane polarization of the E-ray, the upper limit of frequency of the virtual reference grating is increased by a factor of 3, as shown in Table 2.

Practical values of the basic sensitivity of moire interferometry are listed in Table 3. Angle  $\alpha$  is assumed to be  $64^\circ$ , providing sensitivity of 90% of the

Table 1. Theoretical limits for various optical glasses.

Medium	Refractive Index	Theoretical Limit <sup>†</sup>	
		$f_{\max}$ (lines / mm)	Sensitivity (nm / fringe)
Air	1.00	3890	257
Fused Silica	1.46	5680	176
Pyrex	1.48	5760	174
BK7 <sup>*</sup>	1.52	5910	169
SF2 <sup>*</sup>	1.66	6460	155
SF18 <sup>*</sup>	1.73	6730	149
LaSF6 <sup>*</sup>	1.98	7700	130

Note

\* Optical glass designations

† for wavelength  $\lambda = 514\text{nm}$ 

Table 2. Theoretical limits for an optical crystal.

Optical Crystal (TiO <sub>2</sub> )	Refractive Index	Theoretical Limit	
		$f_{\max}$ (lines / mm)	Sensitivity (nm / fringe)
O Ray	2.70	10,510	95
E Ray	3.00	11,670	86

Table 3. Practical limits of sensitivity.

Refractive Medium	Practical Limit of Sensitivity <sup>1</sup> (nm / fringe)		
	$\lambda^2 = 514\text{nm}$	$\lambda^3 = 488\text{nm}$	$\lambda^4 = 442\text{nm}$
Air	286	271	246
Fused Silica	196	186	168
Pyrex	193	183	166
BK7	188	178	162
SF2	172	163	148
SF18	165	157	142
LaSF6	144	137	124
TiO <sub>2</sub> (O ray)	106	100	91
TiO <sub>2</sub> (E ray)	95	90	82

**Notes**

<sup>1</sup> assuming 90% of the theoretical limit, i.e.,  $\alpha = 64^\circ$

<sup>2,3</sup> wavelengths of Argon laser

<sup>4</sup> wavelength of HeCd laser

theoretical limit. The sensitivity is given for three different visible wavelengths of commercially available lasers. As can be seen in Table 3, when LaSF6 is used with  $\lambda = 442\text{nm}$ , the basic sensitivity can be increased by more than 3 times when compared to the basic sensitivity used in the routine practice of moire interferometry, i.e., with  $f = 2400$  lines per mm and sensitivity of  $417\text{nm}$  per fringe order. Furthermore, with the optical crystal, one could achieve an increase of 5 times, to reach about 60% of the sensitivity objective ( $50\text{nm}$  per fringe contour).

## 2.4 Optical Configurations

This section describes three different optical configurations that could be fabricated from the optical glasses introduced above.

### 2.4.1 Configuration 1

Figure 4(a) illustrates configuration 1 schematically. The shaded element is fabricated from optical glass or crystal and it is called an immersion interferometer. The mirrorized surface is analogous to the mirror in Fig. 1. A collimated beam enters through an inclined entrance plane (Fig. 4(a)). The lower portion of the beam impinges directly on the specimen grating while the upper portion impinges indirectly after reflection from the mirrorized surface; they create a virtual reference grating on the specimen.

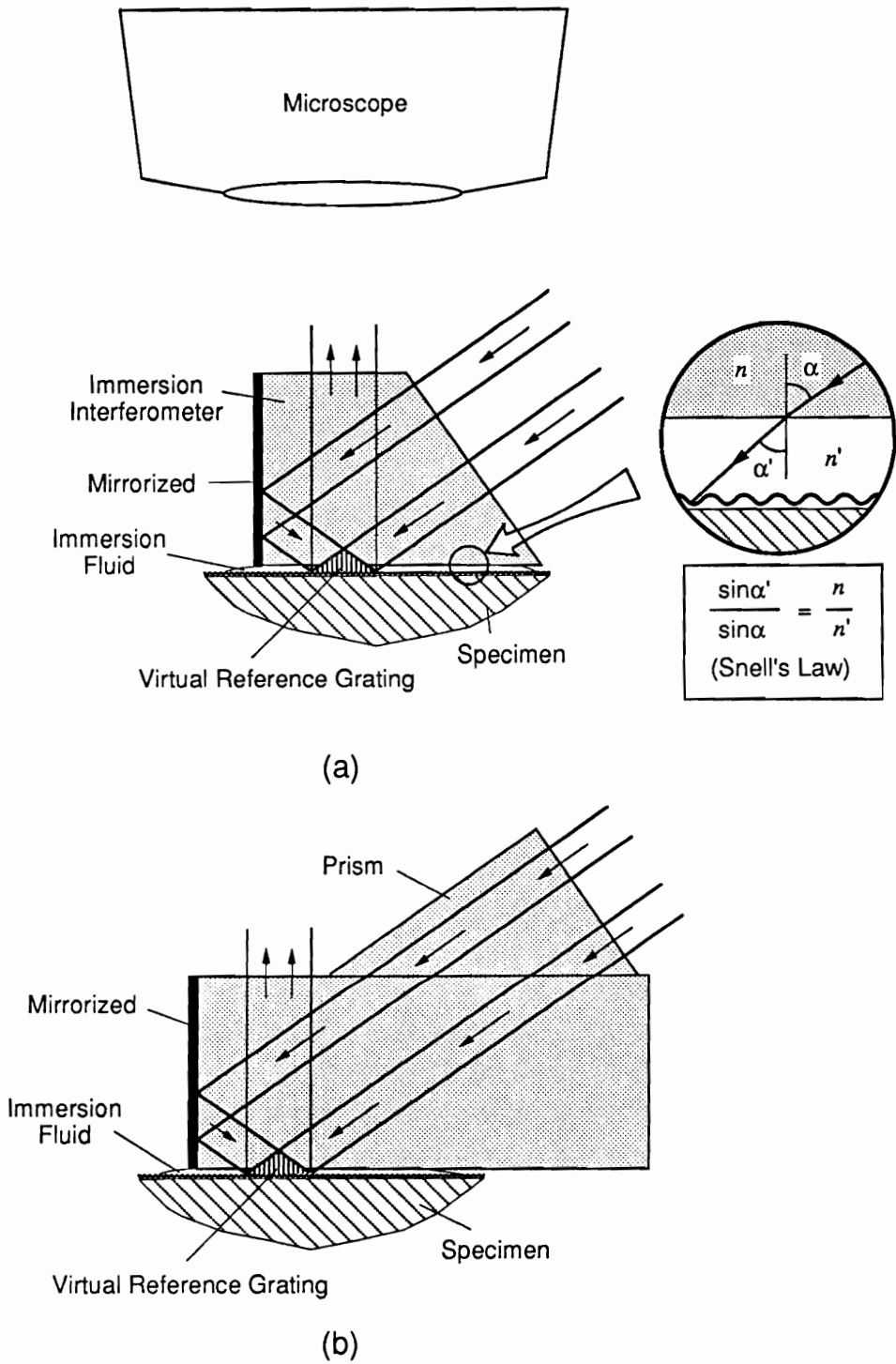


Fig. 4 (a) Configuration 1 and (b) its variation.



The gap between the interferometer and the specimen grating is filled with an immersion fluid to achieve optical contact with the specimen grating. When the refractive index of the immersion fluid is not the same as that of the immersion interferometer, the angles of rays in each media are different from each other, as illustrated in the insert in Fig. 4(a). But, this condition does not alter the frequency of the virtual reference grating. This can be explained from Eq. (13), repeated here,

$$f_m = \frac{2\sin \alpha}{\lambda_m} = \frac{2n\sin \alpha}{\lambda} \quad (13)$$

It is clear that the magnitude of the virtual reference grating frequency,  $f_m$ , is not changed regardless of the refractive index of the fluid because the value of  $n\sin\alpha$  is identically equal to  $n'\sin\alpha'$  according to the law of refraction (see the insert in Fig. 4(a)), and therefore the right-hand term remains unchanged. The same result is obtained from the equations of diffraction and refraction without the conceptualization of a virtual reference grating [42]. A reasonable match of refractive indices of immersion fluid and immersion interferometer is desired, but mismatch of indices can be tolerated until it is so large that the critical angle of complete internal reflection occurs.

A variation of configuration 1 is illustrated in Fig. 4(b) where a prism is attached with an optical cement and one of its surfaces acts as the entrance plane.

The angle of the entrance plane is an important parameter. If the entrance plane is horizontal, the angle  $\alpha$  required to create a virtual reference grating is limited according to the law of refraction. Figure 5(a) illustrates the case for  $n = 1.5$ , where the maximum value of  $\alpha$  is only  $41^\circ$ , corresponding to an incident angle  $\theta_i$  of  $90^\circ$ . Thus, the entrance plane should be inclined to allow the desired angle  $\alpha$ . In addition, the amount of light transmitted into a refractive medium decreases as the incident angle  $\theta_i$  increases. Therefore, in practice, the angle of the entrance plane should be approximately perpendicular to the incident beam. Then,  $\alpha$  could be adjusted in a wide range to accommodate carrier patterns and still achieve a high level of light utilization.

Multiple reflections inside the interferometer is another significant parameter. This is illustrated schematically in Fig. 5(b), where a beam is diffracted by a specimen grating and emerges normal to the specimen. When it arrives at the top surface of the interferometer, some portion of the light is reflected back to the specimen while most of the beam is transmitted. The transmitted light (A in Fig. 5(b)) and the 0<sup>th</sup> order diffraction (A' in Fig. 5(b)) of this returning beam could create an undesired interference pattern, a so-called ghost pattern. For the optical glasses considered here, the reflectance will be 4-10%, depending upon the refractive index. Note that two beams with a 100:1 intensity ratio can produce a discernable fringe pattern with a contrast of 33% of that for pure two beam interference [42]. Thus, the ghost pattern can deteriorate the quality of the moire pattern and should be eliminated.

One solution to cope with the problem is illustrated in Fig. 5(c), where the top surface of the interferometer has an angle with respect to the bottom

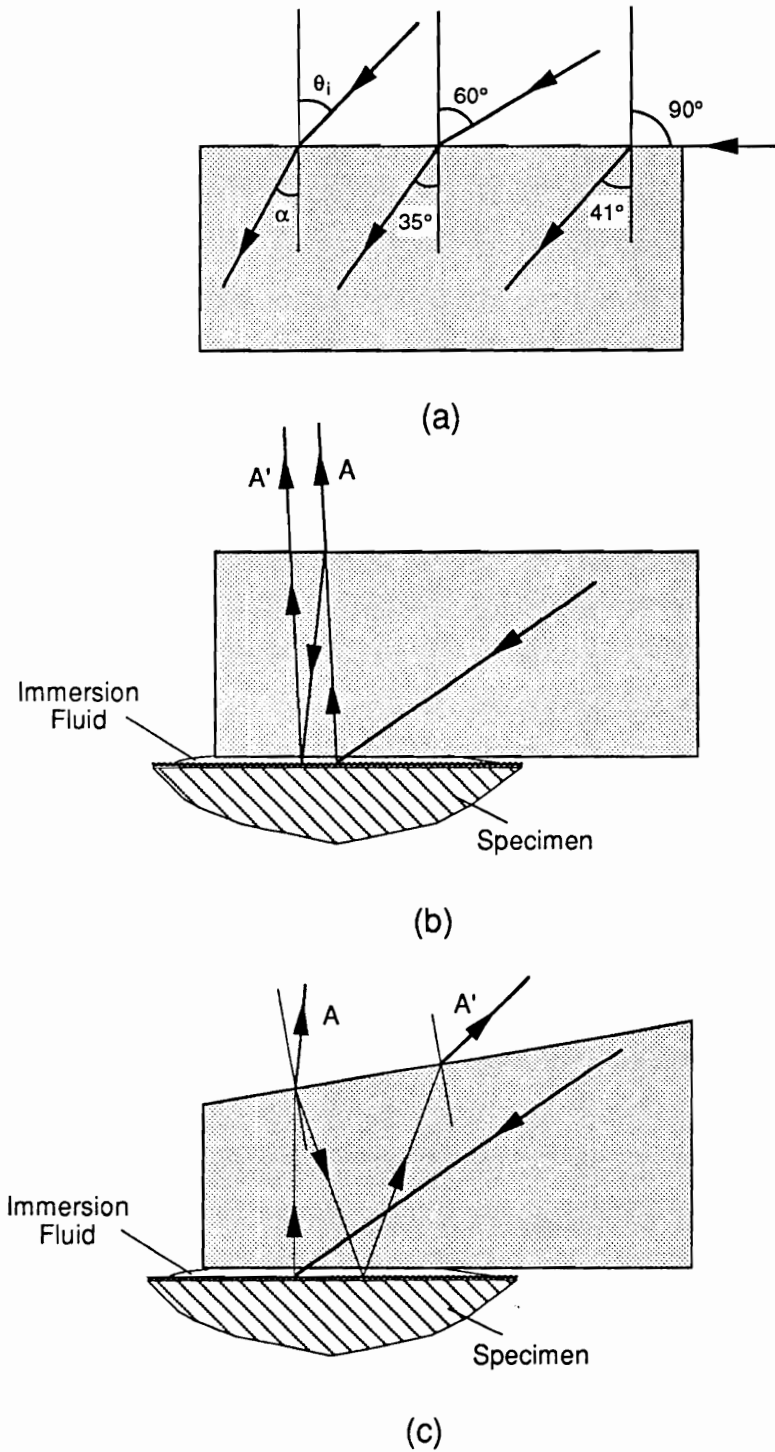


Fig. 5 Illustrations for (a) law of refraction, (b) rays creating a ghost pattern and (c) a solution to eliminate the ghost pattern.

surface. Then, the reflected beam A' will not be captured by the image recording system. However, beam A is also steered due to the wedge angle. Accordingly, this would be a practical solution only if the microscope lens of the image recording system is suitably inclined and has a long working distance.

Another practical way to circumvent the ghost pattern is to apply an antireflection coating to the top surface of the interferometer. With multi-layer dielectric coatings, the reflectance can be reduced to 0.15% which can be ignored in practice. This is the preferred method.

### 2.4.2 Configuration 2

Configuration 2 is basically the same as configuration 1 but, as illustrated in Fig. 6, a collimated beam experiences multiple internal reflections before it strikes the specimen grating. This configuration would be more suitable for systems in which the interferometer must be very thin. This would be the case if the working distance of the lens is not large.

It is interesting to remember that total internal reflection is obtained when incident angles are greater than the critical angle. The critical angle can be calculated from the law of refraction and it can be expressed as

$$\theta_c = \sin^{-1}\left(\frac{1}{n}\right) \quad (14)$$

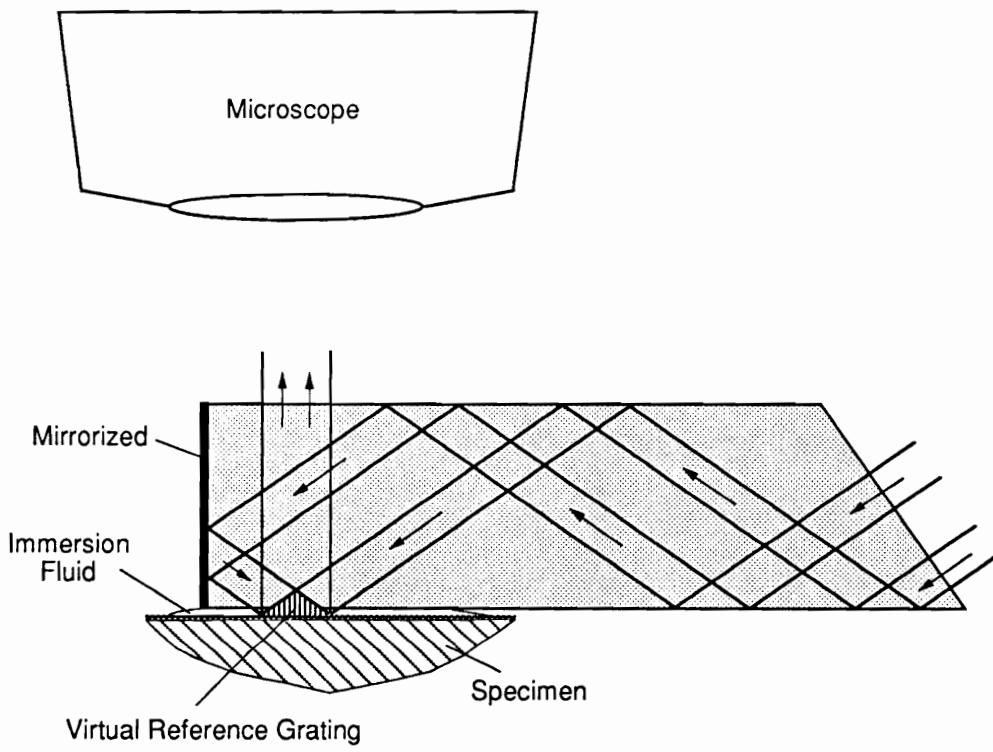


Fig. 6 Configuration 2.

where  $\theta_c$  is the critical angle,  $n$  is the refractive index of the medium, and the external medium is air. For optical glasses considered here, the value of the critical angle is in the range of  $30^\circ$  to  $43^\circ$ . Thus, total internal reflections will occur for the angles considered here, angles of  $50^\circ$  to  $65^\circ$ . Accordingly, the top and bottom surfaces do not have to be mirrorized and the requirements in constructing configuration 2 would be almost the same as those for configuration 1.

### 2.4.3 Configuration 3

Configuration 3 is different from the other two configurations in that a real grating is utilized to achieve a desired angle  $\alpha$ . As illustrated in Fig 7(a), +1 diffraction order from the real grating illuminates a specimen grating in the same way as in configuration 2. If the frequency of the real grating (the so called compensator grating) is the same as that of the specimen grating, the angle of the diffracted beam would be exactly equal to the desired angle  $\alpha$  to create a virtual reference grating on the specimen. The entrance plane for this configuration is the top surface of the interferometer and the modification for the entrance plane is not required.

Configuration 3 is a variation of an achromatic interferometer developed by Post [47] and it has a very important feature. Briefly, the compensator grating permits use of a chromatic light source, or a light source with a relatively broad wavelength spectrum. When a collimated chromatic beam illuminates the compensator grating, it produces exactly the right angle  $\alpha$  in each wavelength

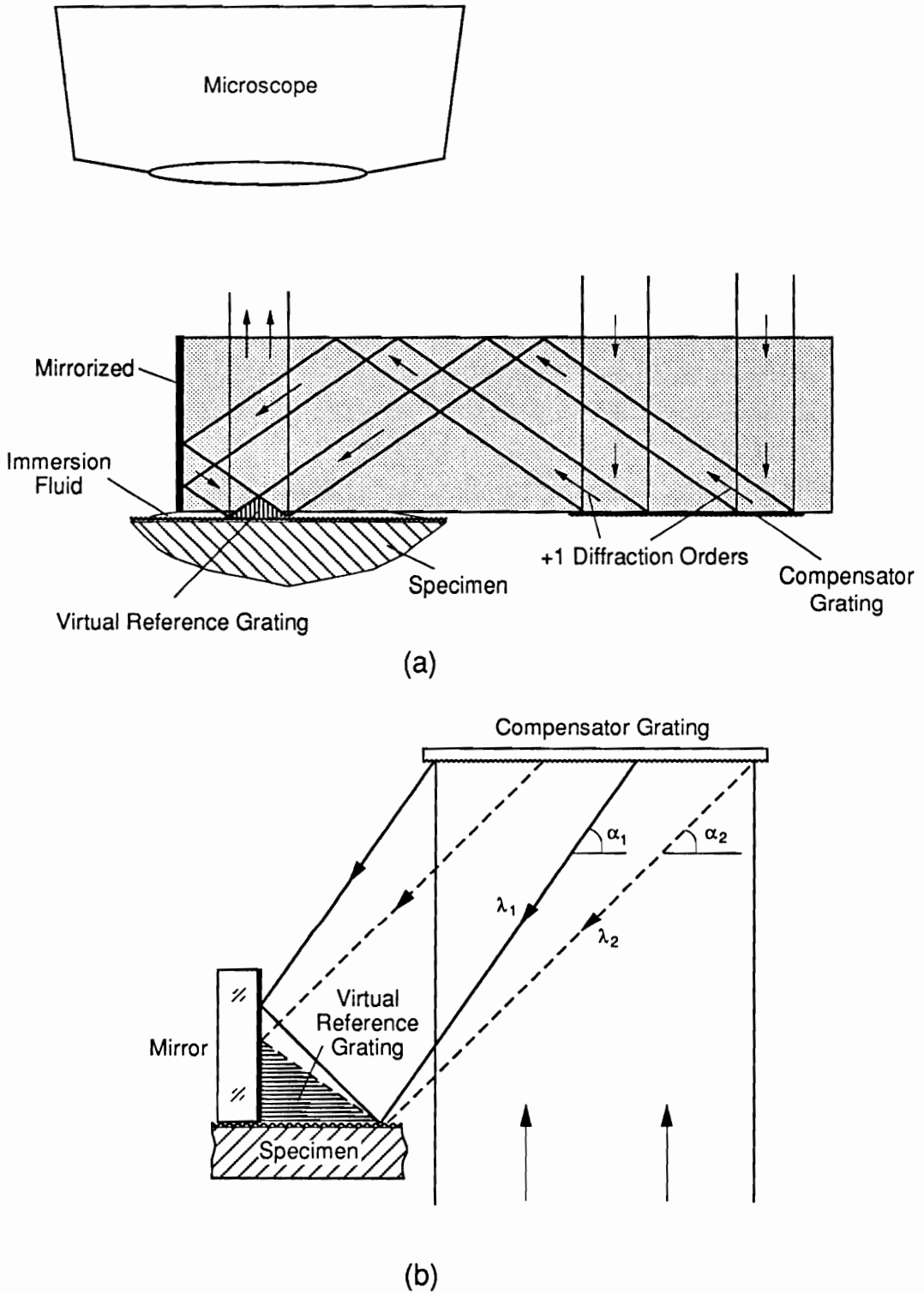


Fig. 7 (a) Configuration 3 and (b) illustration of compensation for chromatic light.

to produce a virtual reference grating with the same frequency on the specimen (Fig 7(b)); in other words, the virtual reference grating created by the chromatic light behaves exactly like that created by a coherent light [47].

Although compensation for chromatic light can be accomplished by using the compensator grating, the requirements on source width, or degree of collimation are not altered.

A laser diode would be a very attractive choice as a light source for this configuration since, apart from its compactness and low cost, it has very narrow physical dimensions compared to other broad-band light sources such as mercury vapor lamps. Currently most laser diodes emit infra-red light, but it is expected that shorter wavelength laser diodes of high power will be available in the near future due to the rapid development in the industry. If a laser diode is used in this configuration, the complete optical system would be extremely small and compact.



## 3.0 MICROSCOPIC MOIRE INTERFEROMETRY

### 3.1 Introduction

A very compact four-beam immersion interferometer was designed and constructed for microscopic viewing. It is a four-beam version of configuration 1, illustrated in Fig. 4(b). It was installed under a microscope and CCD video camera that acted as the image recording (or camera) system. Its configuration made it inherently stable and relatively insensitive to environmental disturbances. This allowed a robust scheme to shift the fringes for step 2.

In this work, BK7 was used as the refractive medium and an argon-ion laser that emits a green light ( $\lambda = 514\text{nm}$ ) was employed as the light source. The refractive index of BK7 is 1.52 for this wavelength. A specimen grating of 1200 lines/mm was employed; its  $\pm 2$  diffraction orders enabled use of a virtual reference grating of 4800 lines/mm.

### 3.2 Enhancement of Sensitivity

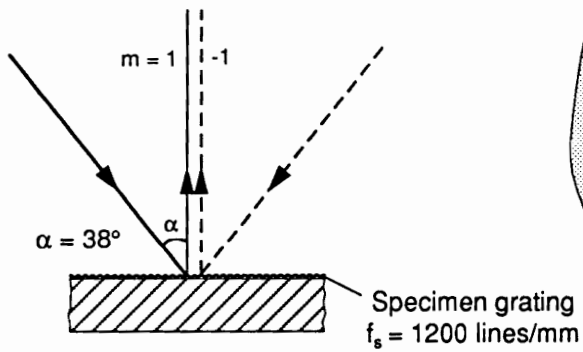
The enhancement of sensitivity by using higher order diffraction beams can be explained by recalling Eq. (8), which shows that the sensitivity is the reciprocal of  $2m$  times the initial frequency of the specimen grating, where  $\pm m$  are the diffraction orders used to produce the moire pattern. Thus, for the given frequency of a specimen grating, the sensitivity can be increased by using

$$\sin\alpha = m\lambda f_s \quad (7)$$

### In Air

$$\lambda = 514 \text{ nm}$$

$$f = 2mf_s = 2400 \text{ lines/mm}$$

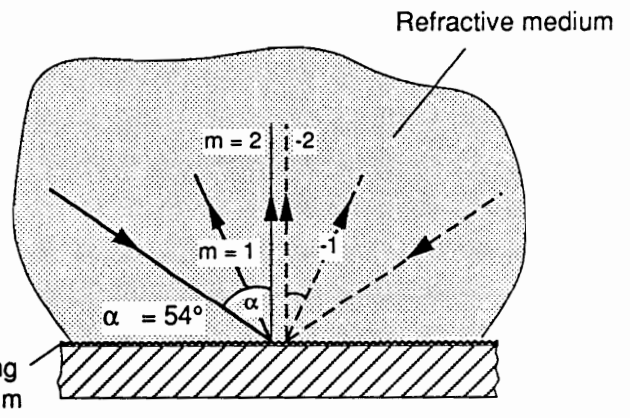


(a)

### In Refractive Medium (BK7)

$$\lambda_m = \frac{\lambda}{n} = 338 \text{ nm}$$

$$f = 2mf_s = 4800 \text{ lines/mm}$$



(b)

Fig. 8 Frequency of virtual reference grating (a) in air and (b) in BK7.

higher order diffraction beams. As can be seen in Fig. 8(a), only  $m = 1$  satisfies Eq. (7) when the frequency of the specimen grating is 1200 lines/mm and the medium is air; with  $m > 1$  in this case, Eq. (7) requires  $\sin\alpha > 1$ . However, in BK7, Eq. (7) is satisfied with  $m = 2$  for the same frequency of specimen grating (Fig. 8(b)) since the wavelength of light is reduced to 338nm in BK7. Thus, the sensitivity is increased by a factor of 2 compared to that of Fig. 8(a). The enhanced sensitivity is 208nm per fringe order. With this basic sensitivity provided from step 1, the sensitivity objective can be achieved (essentially) with a subsequent fringe multiplication factor of only 4.

### 3.3 Immersion Interferometer

The configuration of the four-beam immersion interferometer is illustrated in Fig. 9. The basic description of the interferometer is a glass plate on which two prisms are mounted. The shaded surfaces were coated by vacuum deposited aluminum and they act as the mirror in Fig. 4(b). Two collimated beams  $a$ ,  $b$  enter the interferometer through the prisms and they create two virtual reference gratings for the U and V fields.

Since the interferometer requires accurately perpendicular surfaces of high optical quality, it was cut out of a corner cube reflector (that originally had three perpendicular optical surfaces) and the cut surface was subsequently polished. Figure 10 illustrates the corner cube reflector used here and how the cut was made. The perpendicularity of the three optical surfaces of the corner cube was accurate to a tolerance of three arc seconds. Since corner cubes are

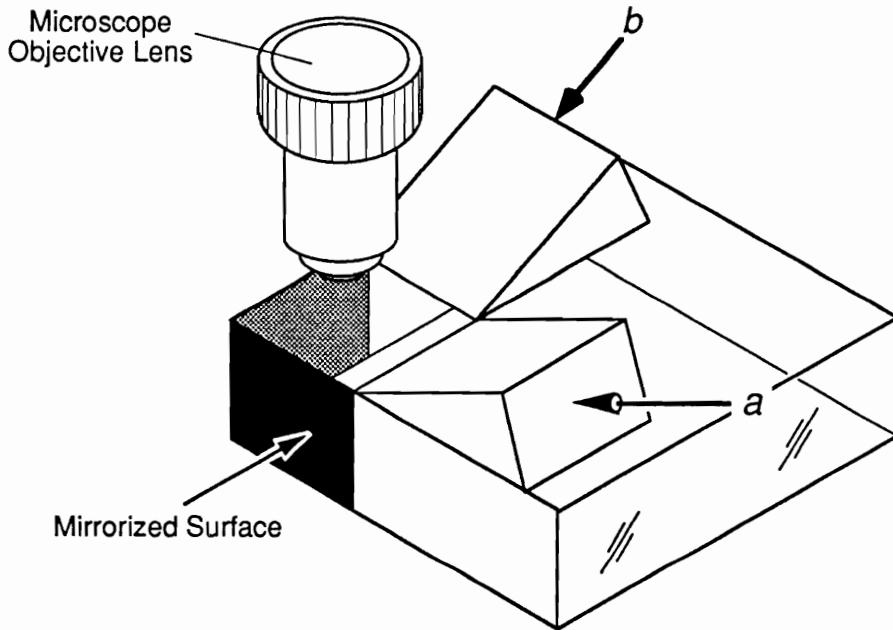


Fig. 9 Four-beam immersion interferometer.

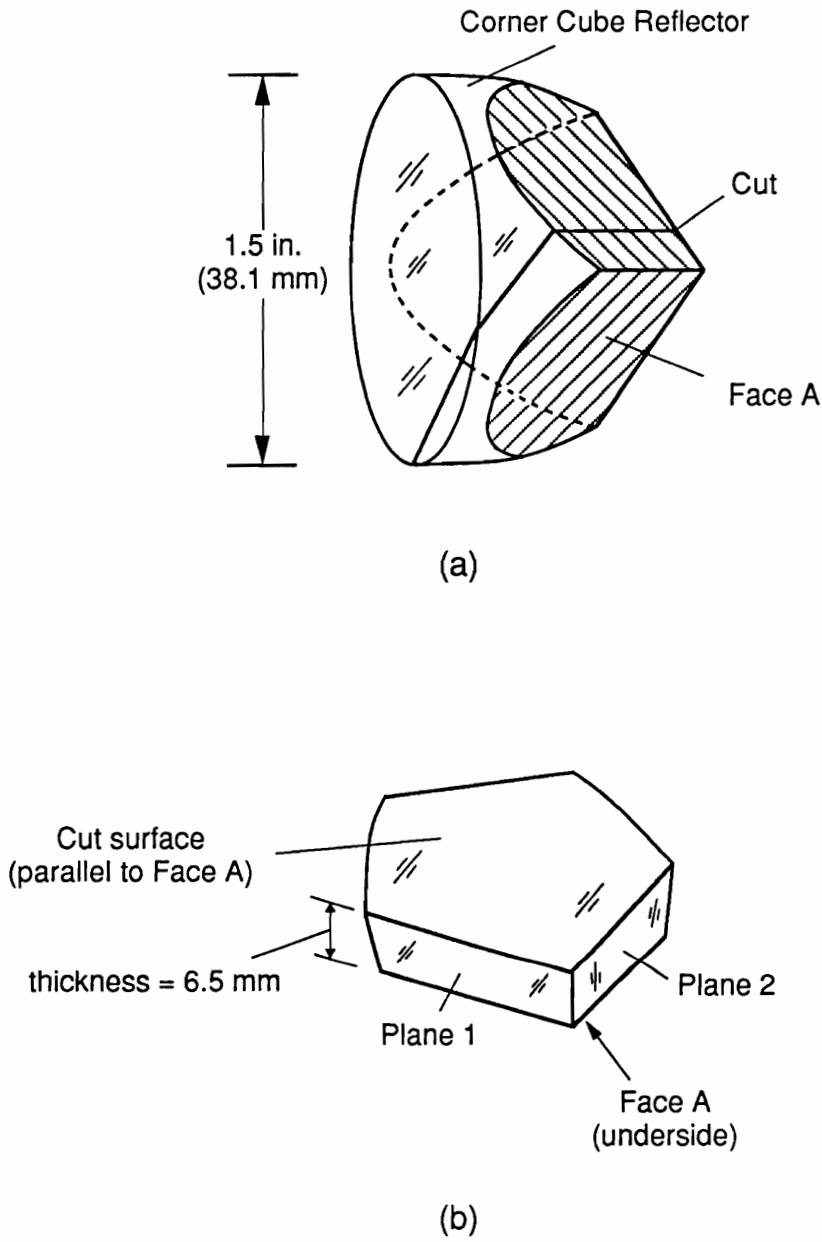


Fig. 10 Fabrication of the main element of the immersion interferometer.

manufactured in high volume and therefore they are inexpensive, this was an economical approach. To complete the interferometer, two prisms were bonded to the main element with an optical cement and plane 1 and 2 were mirrorized by vacuum deposition of aluminum.

A microscope objective lens that was specially designed to have a large working distance was chosen. A good focus over the entire region of interest was obtained. This objective lens has another special feature. It was infinitely corrected, which means it projects a good image regardless of the distance to the image. Accordingly, magnification could be increased merely by increasing the lens to image distance. Since a CCD video camera was used, the normal specification of magnification is not meaningful. Instead, object size per TV frame is meaningful. Good results were obtained for object fields varying from 0.6mm x 0.6mm to 0.1mm x 0.1mm, with images displayed in 480 x 480 pixel format.

Multiple reflections between a surface of the microscope objective lens and the specimen surface created an undesired interference pattern of ghost fringes which deteriorated the quality of the moire fringes. This noise was virtually eliminated by coating the bottom surface of the interferometer with black paint, except for a small region for viewing. The small region acted as an aperture to minimize the amount of light captured by the microscope so that the influence of the noise became negligible.

## **4.0 FRINGE SHIFTING**

### **4.1 Introduction**

Fringe shifting has been used extensively in photoelasticity, especially by the Tardy method [48]. Fringe shifting has been advocated for geometric moire [49,50], but few applications appear in the literature. In holographic interferometry, the heterodyne method [51] and phase stepping method [52, 53] are related to (but not the same as) the fringe shifting used here, where the phase of a reference beam is changed to shift fringes. Patorski [54] suggested a fringe-shifting method for moire interferometry wherein the shift is controlled by the polarization of light.

In this work, a simple mechanical scheme to shift the fringes in moire interferometry was developed and implemented. In spite of its simplicity, the scheme provided excellent stability and accuracy. This scheme will be discussed in detail below.

### **4.2 Fringe Shifting**

The method can be explained by an analogy. In geometric moire, fringes appear where two sets of grating lines intersect [49]. When one of the gratings is translated, these intersection points are also shifted. This is illustrated in Fig. 11 where one of the superimposed gratings is translated horizontally by half

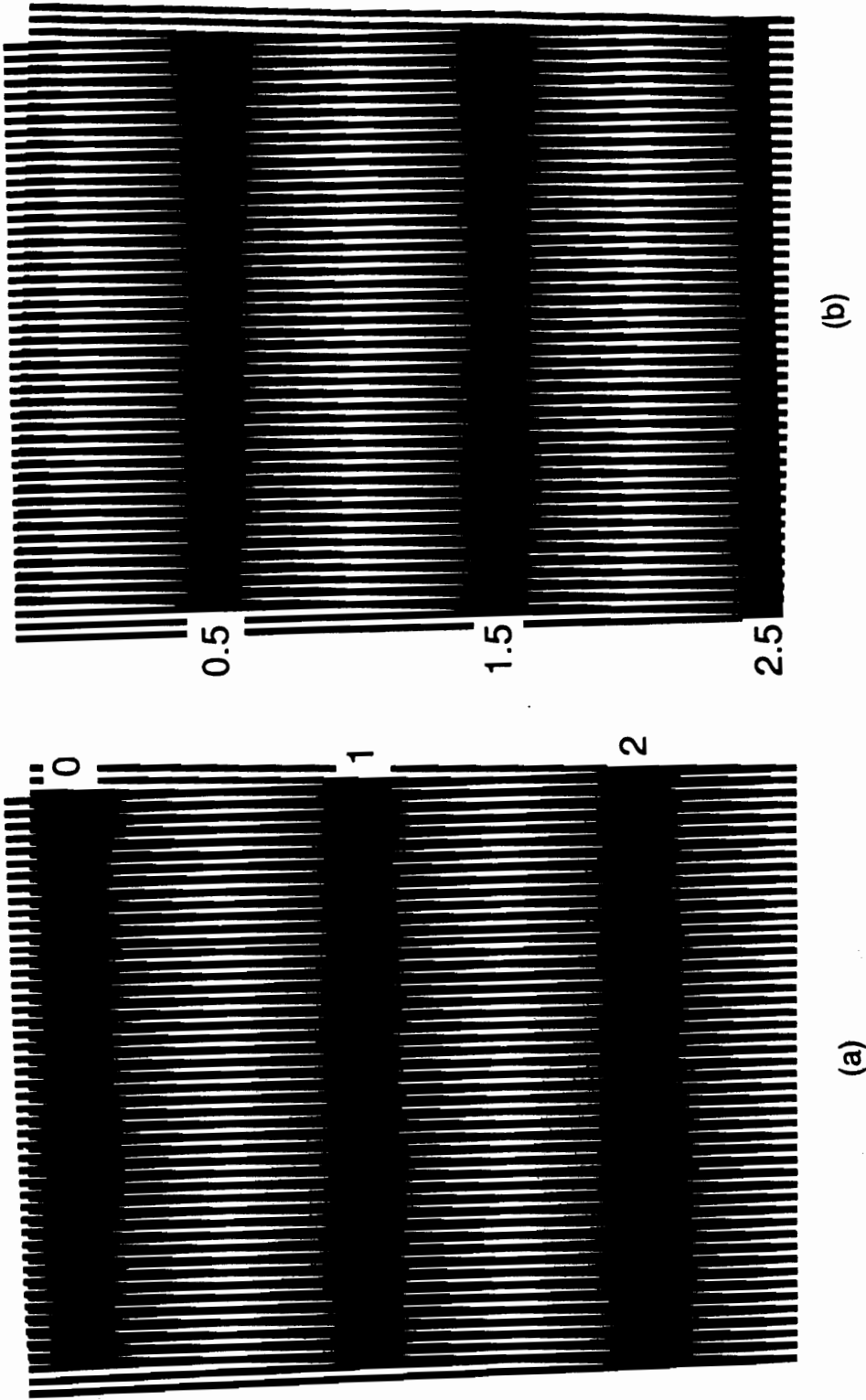


Fig. 11 Illustration of fringe shifting in geometrical moire. (a) an original pattern (b) a shifted pattern where the reference grating is translated horizontally by half of its pitch.



of its pitch and fringes are shifted by the same fraction of a fringe order. Analogous to this, fringes in moire interferometry can be shifted by translating the virtual reference grating.

Analytically, fringe shifting in moire interferometry can be explained from Eq. (8), repeated here,

$$U(x,y) = \frac{1}{2mf_s} \left( N(x,y) - \frac{\delta}{\lambda} \right) = \frac{1}{f} \left( N(x,y) - \frac{\delta}{\lambda} \right) \quad (8)$$

where  $\delta$  is the optical path length difference between the two incident beams. It is clear that a change of  $\delta$  can shift the fringe order uniformly over the field; it can move the center of a fringe to any desired point in the field. Accordingly, subsequent changes of  $\delta$  by a fraction of a wavelength, say  $\lambda/\beta$ , will result in a subsequent change of fringe order at every point in a moire pattern by the same fraction, i.e.,  $\Delta N = 1/\beta$ . Note that the distribution of displacements throughout the field is imbedded in  $N(x,y)$ , while the positions of fringe maxima and minima depend upon  $\delta$ .

The change of  $\delta$  is achieved by altering the path lengths of the two incident beams relative to each other. Analogous to geometric moire, an optical path length change of one of the beams by a fraction of a wavelength is equivalent to a shift of the virtual reference grating by the same fraction of its pitch.

Equation (8) is very general. When the light propagates in a refractive medium, the relationship is

$$U(x,y) = \frac{1}{f_m} \left( N(x,y) - \frac{\delta^*}{\lambda_m} \right) \quad (8')$$

where  $\delta^*$  is the difference of mechanical path lengths of the two interfering beams and  $\lambda_m$  and  $f_m$  are the wavelength and virtual reference grating frequency in that medium.

### 4.3 Fringe Shifting Scheme

The method is illustrated schematically in Fig. 12, where the virtual reference grating is shifted by translating the immersion interferometer mechanically. This is done by controlling the piezoelectric actuator that is directly connected to the glass interferometer. Physically, this scheme can be explained by Fig. 13. Rays A and B, separated by the mirrorized surface, travel unique path lengths when they meet at a point P on the specimen. The path length difference determines the state of constructive or destructive interference at P. If the interferometer is translated with respect to the specimen grating by a distance  $d$ , the ray A still strikes the same point P on the specimen without any change of the path length. However, the ray that reaches point P after translation is ray B'. Note that the path length of ray B' is changed from that of B by distance  $a+b$  (Fig. 13).

The path length change can be calculated by trigonometry and can be expressed as

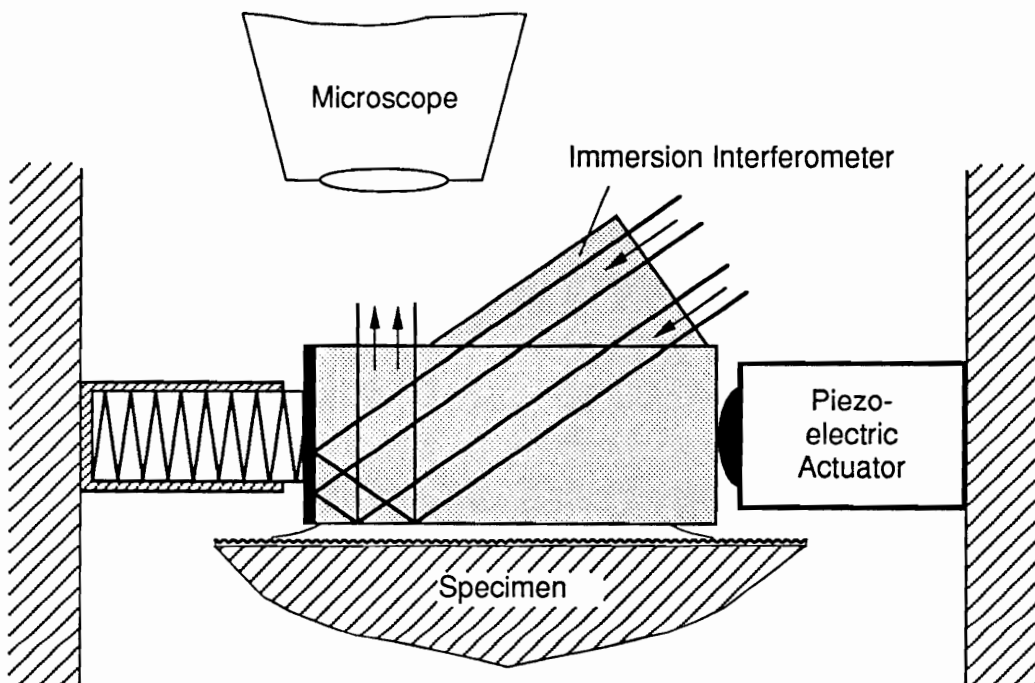


Fig. 12 Schematic diagram of fringe shifting scheme.

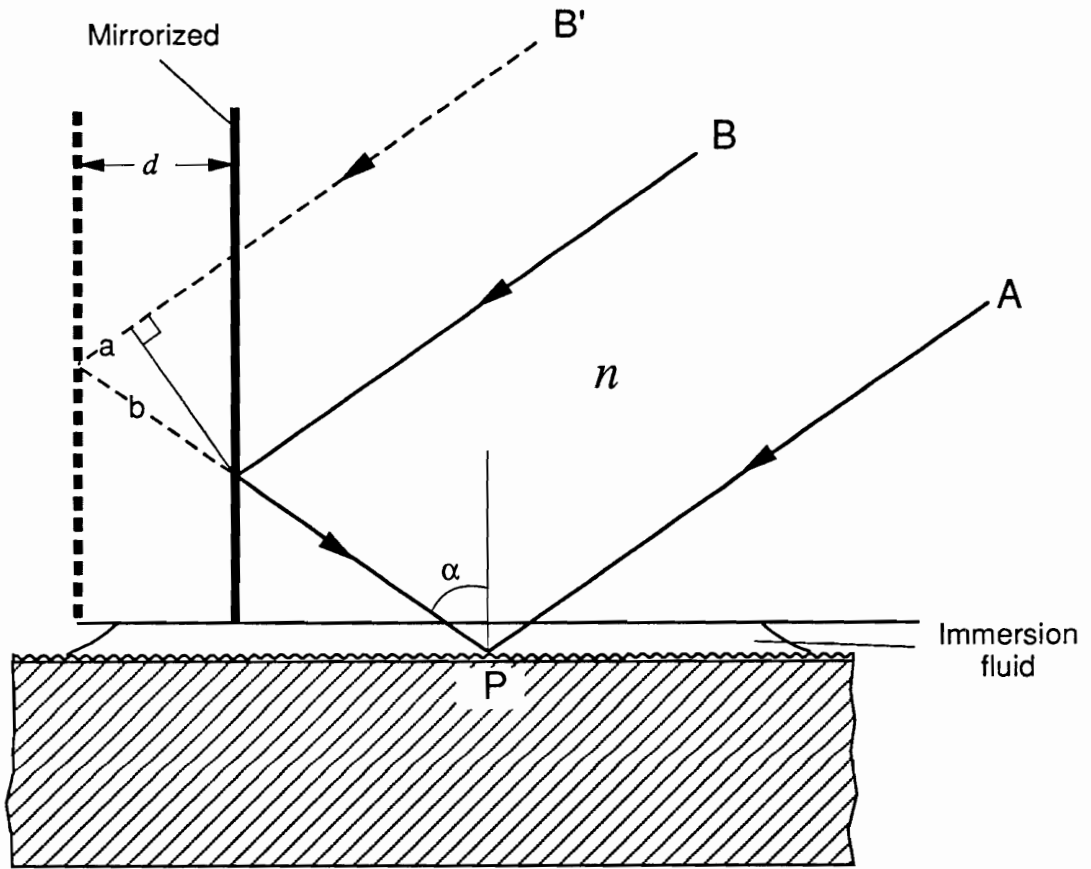


Fig. 13 Physical explanation of shifting scheme.

$$\delta^* = a + b = 2d\sin\alpha \quad (15)$$

Let  $d$  be a fraction of the pitch of the virtual reference grating. That is,

$$d = \frac{p}{\beta}, \quad \beta = 1, 2, 3, \dots \quad (16)$$

where  $p$  = pitch of the virtual reference grating  $= \frac{1}{f_m} = \frac{\lambda_m}{2\sin\alpha}$ .

Then, from Eqs. (15) and (16), we get

$$\delta^* = \frac{2p}{\beta} \sin\alpha = \frac{\lambda_m}{\beta} \quad (17)$$

Thus, when the interferometer is translated by a fraction of the pitch of the virtual reference grating, then the path length change of the two beams at point P is the same fraction of the wavelength. Returning now to Eq. (8'), the result is a change in fringe order everywhere in the field by  $\Delta N = 1/\beta$ . Translation of the interferometer by  $p/\beta$  shifts the fringe order by  $1/\beta$ . Referring back to Fig. 2, it is important to note that the intensity distribution of the basic moire pattern (represented by curve N (step 1)) is shifted by  $N/\beta$ .

## 4.4 Translation and Calibration

Figure 14(a) illustrates the physical shape of the translation device with the immersion interferometer attached. The displacement (or force) generated by the piezoelectric actuator deflects the flexible arms of the actuator holder. This deflection translates the interferometer with respect to the specimen grating, as illustrated in Fig. 14(b) where the deflection is much exaggerated. Since the direction of motion is  $45^\circ$  from the x, y axes, a displacement of  $\sqrt{2}p/\beta$  is required for each fringe shift. The calibration for fringe shifting of the U and V field was identical.

The apparatus was calibrated by a closed-loop system. Its block diagram is illustrated in Fig. 15. The system consists of a piezoelectric actuator, D/A converter, programmable DC amplifier and hardware components for image processing. The piezoelectric actuator (Model PZ-30 by Burleigh) used here operates in a high voltage range (0-1000V) and its maximum traveling distance is  $5\ \mu\text{m}$ . Although a traveling distance of less than  $1\ \mu\text{m}$  was actually required, the larger maximum travelling distance allowed use of the actuator near the center of its traveling range. This is important to avoid non-linearity and hysteresis. A D/A converter board (Model DAC-02 by Metrabyte) was installed in a personal computer (IBM PS2, Model 30 286) to generate 0-5V analogue output. The analogue output provided the input for a programmable DC amplifier, which amplifies the small voltage input to the desired voltage level for the piezoelectric actuator. The resolution of the system was governed by the resolution of the D/A converter, which has 12 bit resolution to yield an error bound of  $\pm 1.22\ \text{mV}$  in the output signal. The programmable DC amplifier

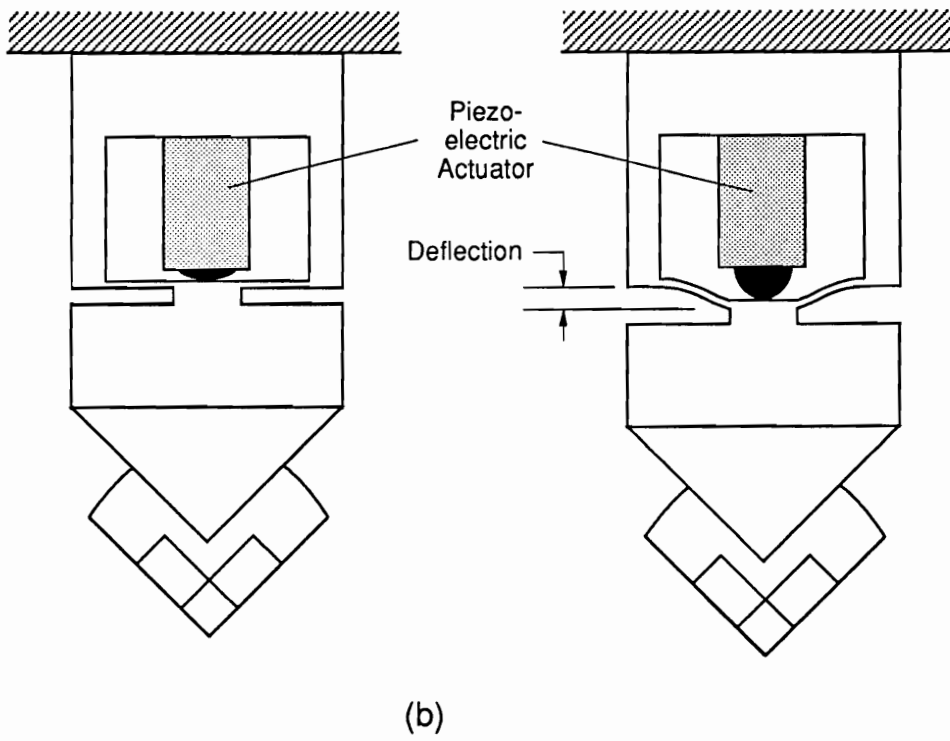
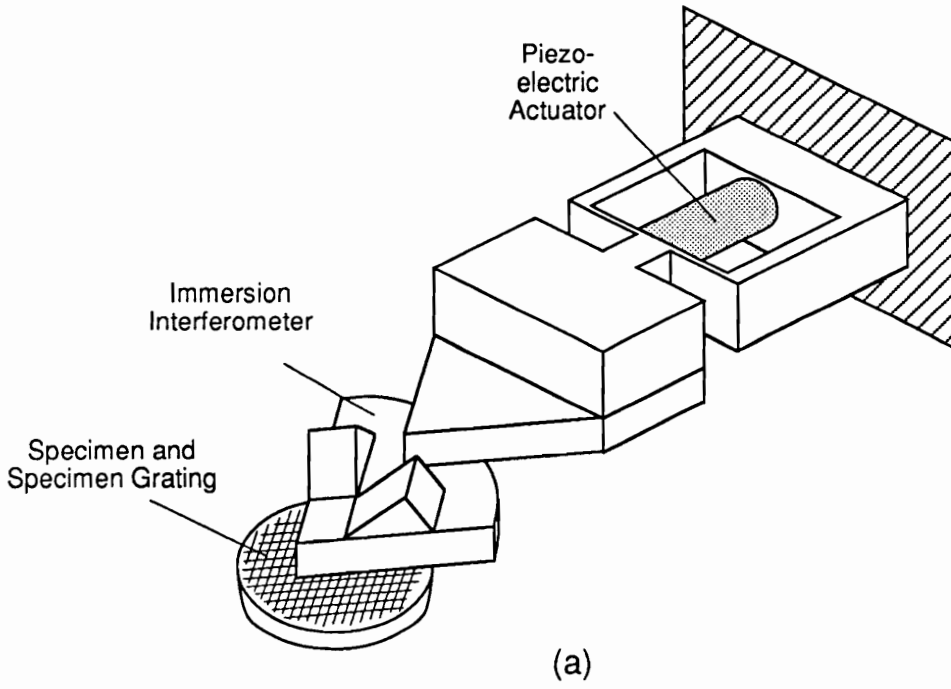


Fig. 14 The translation device.

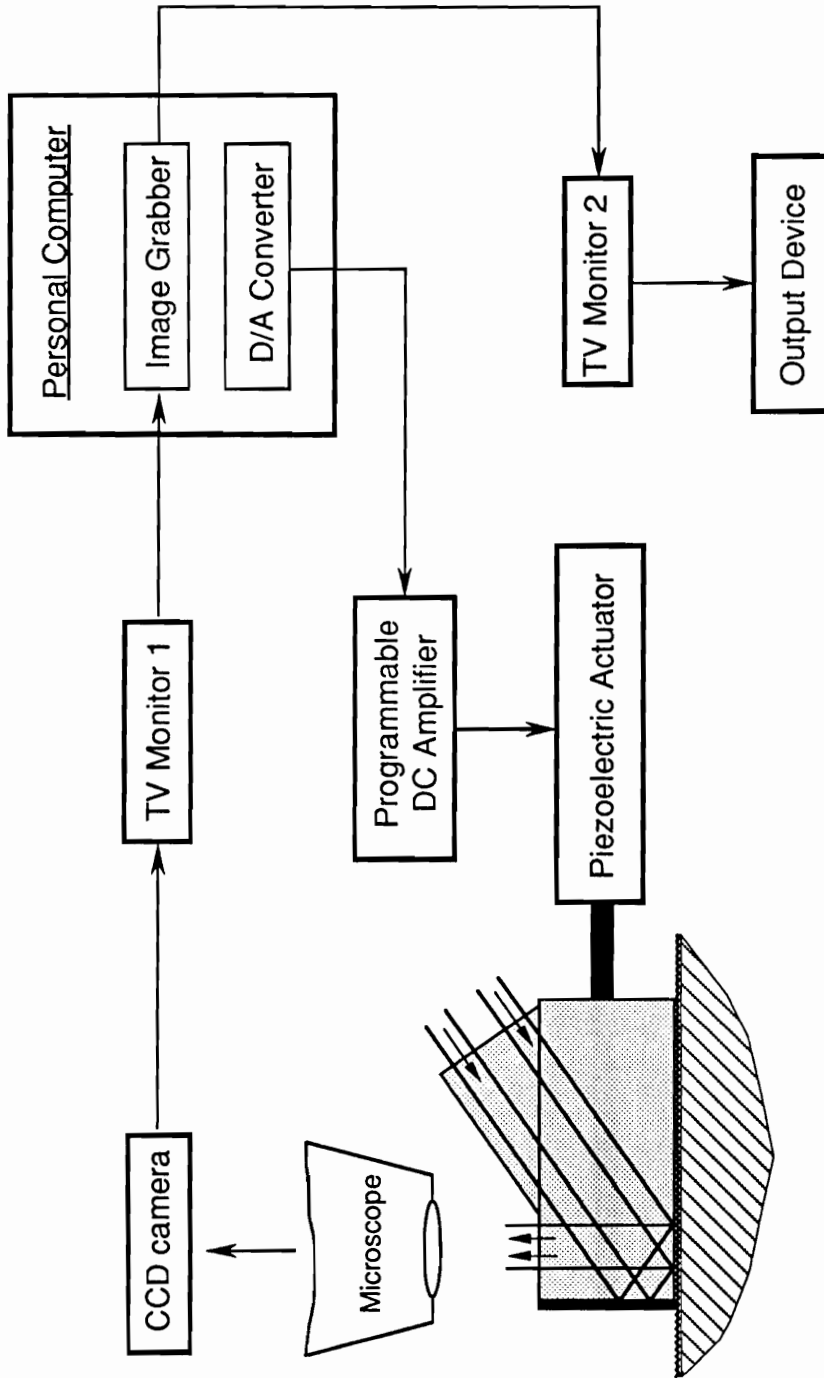


Fig. 15 A block diagram of apparatus for calibration.



(Model PZ-70/70M by Burleigh) has two important features, a DC bias of 0-1000V and a variable gain of 0-200. In the calibration, the DC bias was set at 450V and a gain of about 30 was used. The final error bound of the voltage output after being amplified was  $\pm 37$  mV, which is the error bound for the D/A converter multiplied by the gain used. This corresponds to an error of less than 1nm in the traveling distance of the actuator.

Figure 16 illustrates a flowchart for the calibration and fringe shifting process. The calibration was performed in two steps, initial and fine calibration. In the initial calibration, the desired maximum digital input was specified and the variable gain was slowly increased until a shifted fringe was superposed onto the original pattern ( $\Delta N = 1$ ). Thereafter, the gain remained fixed. Next, in the fine calibration, the original image was captured and digitized. Then, the shifting voltage for  $\Delta N = 1$  was input and the shifted image was also captured and digitized. The original image was subtracted from the shifted one and the histogram of the resulting image was generated. This process was repeated with slightly changed shifting voltages as input until the subtracted images became null, that is, when the two images were identically the same.

Subsequently, a series of fringe-shifted patterns were captured and digitized with fringe shift increments of  $1/\beta$ . Excellent linearity and repeatability of the fringe shifting was achieved after the calibration, as evidenced by tests using rigid-body rotation of the specimen. Since it took only 1/30 second to digitize one frame, shifting and grabbing a series of shifted patterns were performed within a fraction of a second.

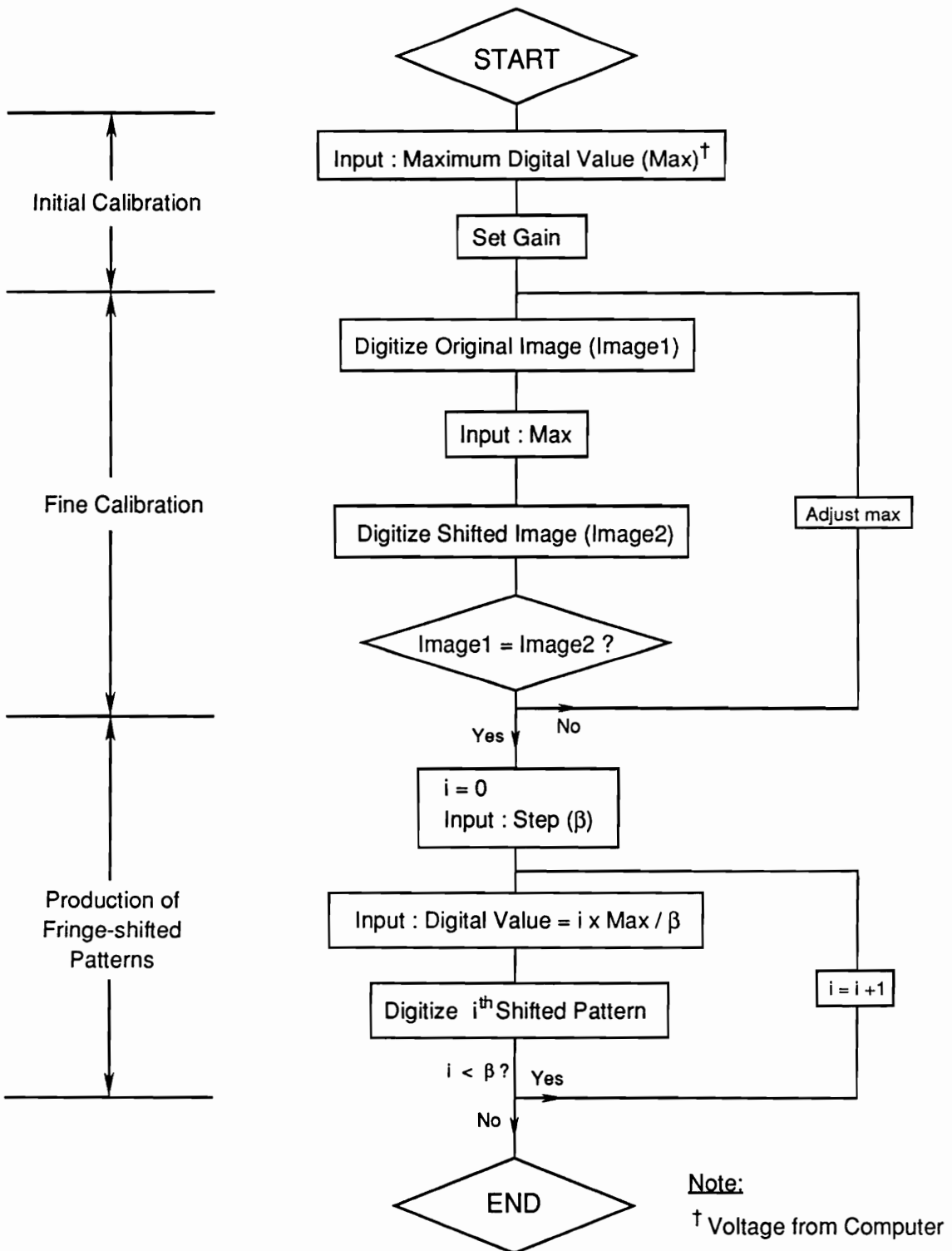
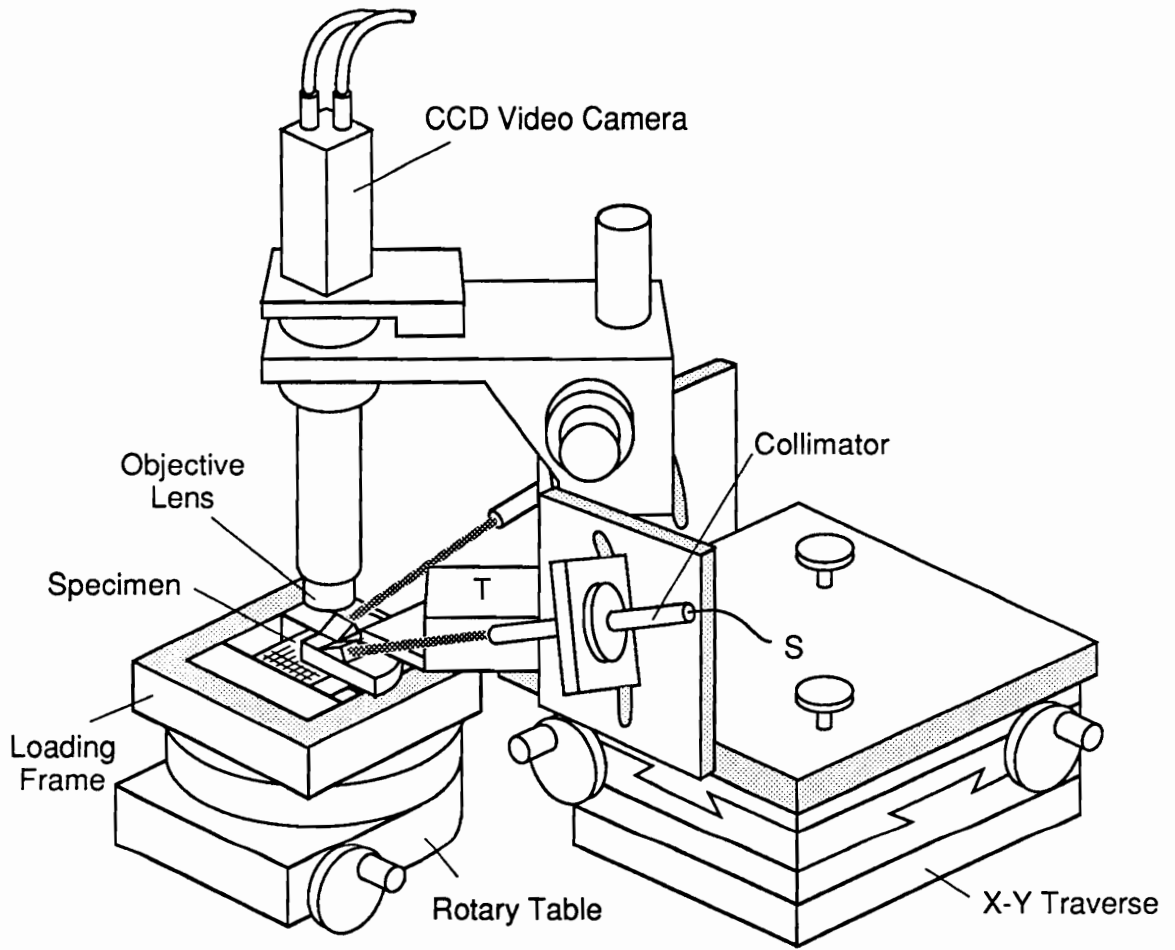


Fig. 16 A flow chart for the calibration and fringe shifting process.

## 5.0 MECHANICAL CONFIGURATION OF THE APPARATUS

The complete optical arrangement is illustrated in Fig. 17. The specimen (with its specimen grating) is mounted in a loading fixture, which in turn, is mounted on a rotatory table for fine adjustments of angular orientation. The immersion interferometer is connected to a translation device (Fig. 14) to move it (relative to the specimen) by predetermined fractions of the pitch of the virtual reference grating. The imaging or microscope system is comprised of a 10x long-working-distance infinity-corrected microscope lens and a CCD video camera (without lens); the magnification is adjusted by changing the lens-to-camera distance. Illumination is conducted by single-mode polarization-preserving optical fibers from an argon-ion laser to collimators that provide 5mm diameter input beams to the interferometer. The collimators are attached to rotatable fixtures to vary the angle of incidence and thus accommodate large carrier patterns of extension when needed. The interferometer, illuminators and microscope are all connected to a heavy-duty x,y traverse to position the system over the desired portion of the specimen. Ancillary equipment includes a power supply to drive the piezoelectric actuator, a personal computer with a frame grabber board and TV monitors.



S : Optical Fiber from Laser Light Source  
T : Translation Device for Fringe Shifting

Fig. 17 The optical and mechanical assembly.

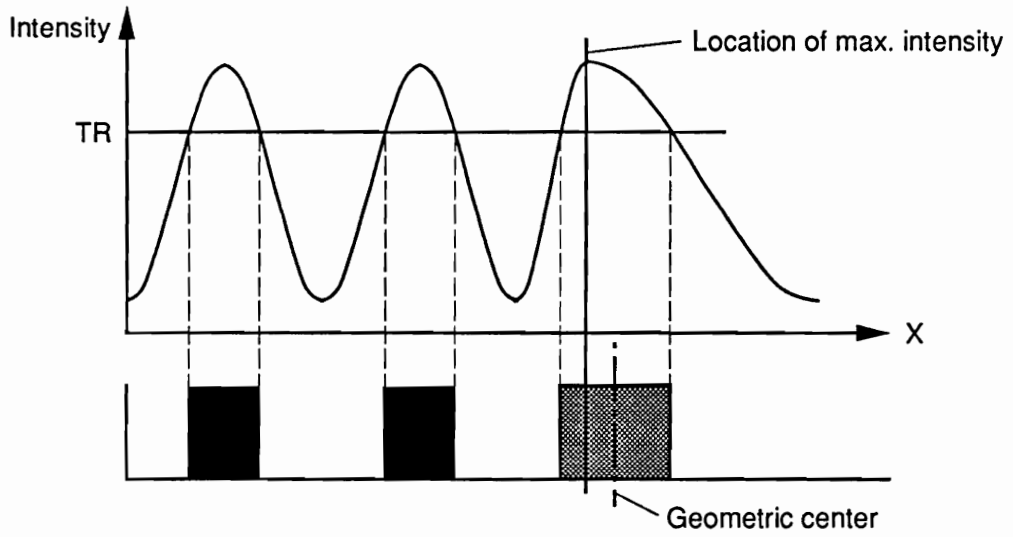
## 6.0 FRINGE SHARPENING AND MULTIPLICATION

### 6.1 Introduction

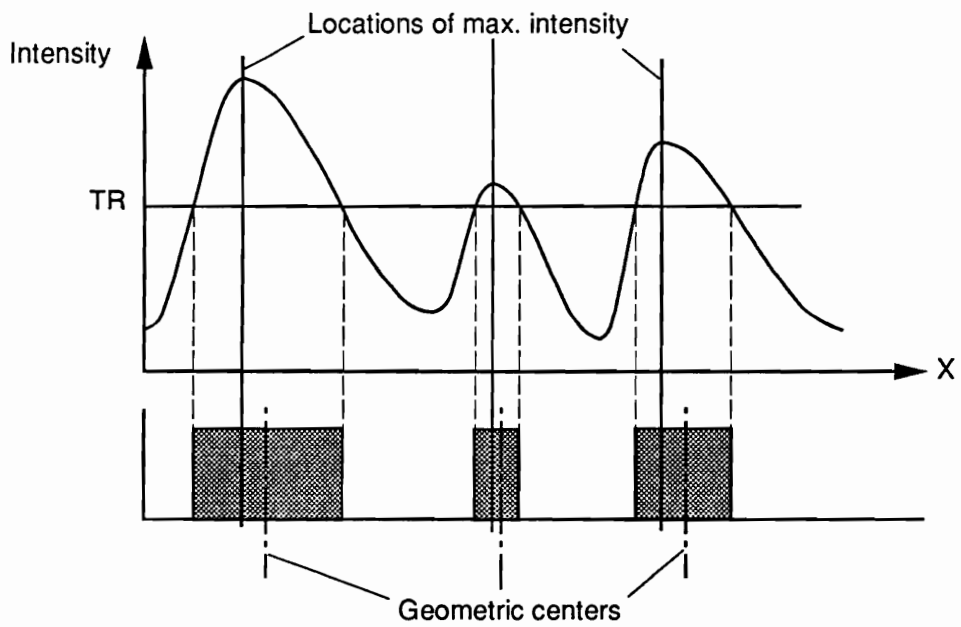
Digital image processing will be used in step 2 to sharpen a series of fringe-shifted patterns and combine them into a composite contour map. These patterns are obtained by sequential shifts of the immersion interferometer by a constant increment, say  $g/\beta$  where  $g$  is the pitch of the virtual reference grating. This shifts the moire fringes by the same fraction of a fringe order; in terms of phase, the fringes are shifted by  $2\pi/\beta$  and these patterns will be called  $2\pi/\beta$ -shifted patterns.

Since the width of fringes limits the number of patterns in the composite map, fringe sharpening was necessary to maximize the number of fringe contours. Digital image processing was utilized to cope with this problem, wherein very thin fringe contours were extracted and they were combined together.

A simple and direct solution for obtaining thin fringe contours would seem to be a process of determining the geometric center of fringes after binarizing the images. In practice, however, such a process could lead to serious errors. This is illustrated in Fig. 18(a), where a single grey level (threshold value) is picked for the entire image, setting the pixels to be black if their values are greater than the threshold value or to be white otherwise; then, the geometric centers of the dark fringes can be determined and traced. In the



(a)



(b)

Fig. 18 Illustration of intensity distributions of moire patterns and the corresponding binary images.

usual case of nonuniform displacement gradients (nonuniform strain fields), the geometric center of a dark fringe deviates from the location of intensity maxima as illustrated in Fig 18(a).

Clearly, the deviation of the geometric center from the location of the intensity maxima is a function of the threshold value used. The errors might become insignificant when a high value of threshold can be used. However, if the illumination or the quality of the specimen grating is not uniform over the region of interest, in other words, if the grey levels corresponding to the intensity maxima vary over the region, a relatively low value of threshold must be used to obtain fringes over the field. That condition is illustrated in Fig. 18(b), in which case the variation of the deviation would be significant. Such a variation would result in substantial error in the determination of strains.

Furthermore, the slope of the intensity distribution of the moire pattern is zero at the intensity maxima. Thus, the certainty of finding the real location of intensity maxima would be dramatically decreased when high frequency noise modifies the intensity distribution.

In this chapter, two very effective image processing schemes will be introduced to circumvent the problems. The influence of nonuniform illumination and optical noise is eliminated and very thin fringe contours are obtained. The schemes developed here are much less computer intensive compared to the currently popular image processing techniques where fractional fringe orders are sought at each pixel. In addition, they offer superior reliability because all data are taken at points where the intensity varies very rapidly. These schemes will be discussed in detail below.

## 6.2 Scheme 1

With this scheme, a series of sharpened fringe contours are obtained from  $\beta$  fringe-shifted patterns. They are combined to produce a fringe contour map with fringe multiplication by a factor of  $\beta$ .

The scheme will be illustrated first for an idealized case, where optical noise is zero. Consider a pair of moire patterns: the original pattern and its complementary pattern ( $\pi$ -shifted pattern). The intensity distributions of those patterns can be expressed as

$$I(x,y) = I_1 + I_2 + 2\sqrt{I_1 I_2} \cos \phi(x,y) \quad (18)$$

$$I_c(x,y) = I_1 + I_2 - 2\sqrt{I_1 I_2} \cos \phi(x,y) \quad (19)$$

where  $I$  is the intensity distribution of the original pattern,  $I_c$  is the intensity distribution of the complementary pattern,  $I_1$  and  $I_2$  are the intensities of the two beams that produce the moire pattern, and  $\phi$  is the phase difference between the two beams;  $\phi$  represents the fringe order  $N$  at each point of the moire pattern, such that

$$\phi = 2\pi N \quad (20)$$

The curves of  $I$  and  $I_c$  are illustrated in Fig. 19(a) for the general case in which  $N$  and  $\phi$  vary nonuniformly along a line  $x$  in the moire fringe pattern.



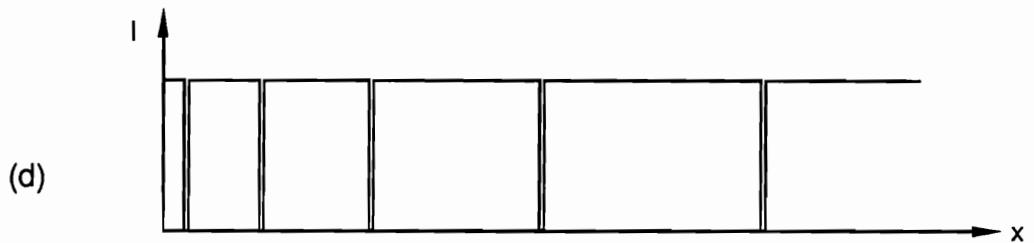
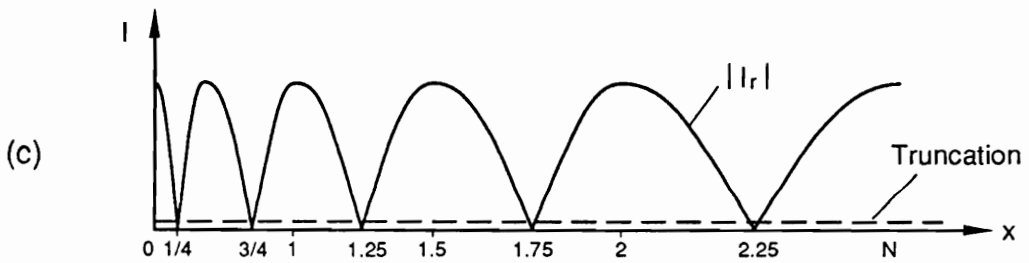
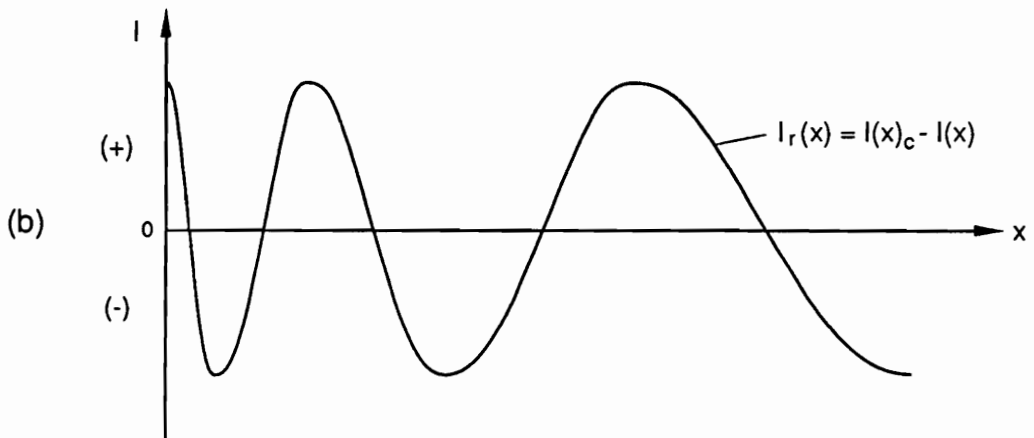
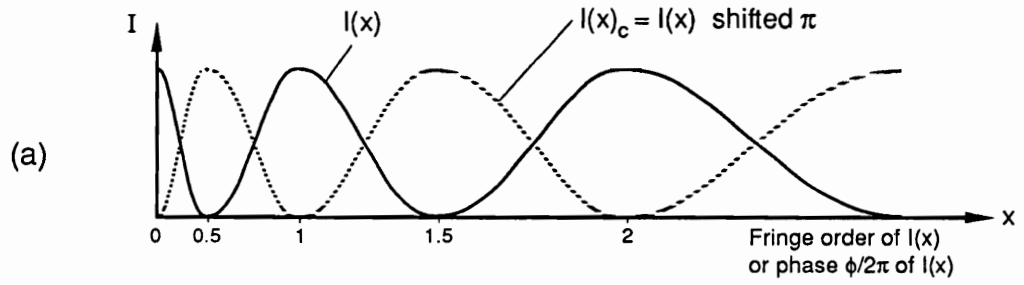


Fig. 19 Illustration of scheme 1 for an idealized case.

If these intensity distributions are captured by a video camera and the intensities at every pixel are converted to digital form, they can be subtracted to give

$$I_r(x,y) = I(x,y) - I_c(x,y) = 4\sqrt{I_1 I_2} \cos \phi(x,y) \quad (21)$$

This is plotted in Fig. 19(b). The absolute value  $|I_r(x,y)|$  is readily calculated for each data point and the resultant distribution is plotted in Fig. 19(c).

The procedure produces highly sharpened fringe contours with minima at the quarter-fringe-order points  $N = 0.25, 0.75, 1.25, 1.75, \dots$ . These will be called the quarter points. In addition to the sharpening, two minima occur for each fringe order of the original moire pattern,  $I(x,y)$ . As a final step in manipulating the data, the intensities are binarized by truncation near  $|I_r(x,y)| = 0$ . The result is the intensity distribution of Fig. 19(d), which represents narrow dark fringes on a bright background.

The process is illustrated in Fig 20 on a whole field basis. The sequence shows the moire pattern and its complement, the subtracted pattern, and the highly sharpened fringe contours of the truncated intensity distribution. The effectiveness of sharpening and doubling of fringes is clearly evident.

Although these data were recorded with a 256 grey level capacity, it was printed out in only a few grey levels. Also, it is evident that optical noise exists in the basic patterns but the results are independent of the noise. The sensitivity to noise in the input beams is expressed by the following analysis.

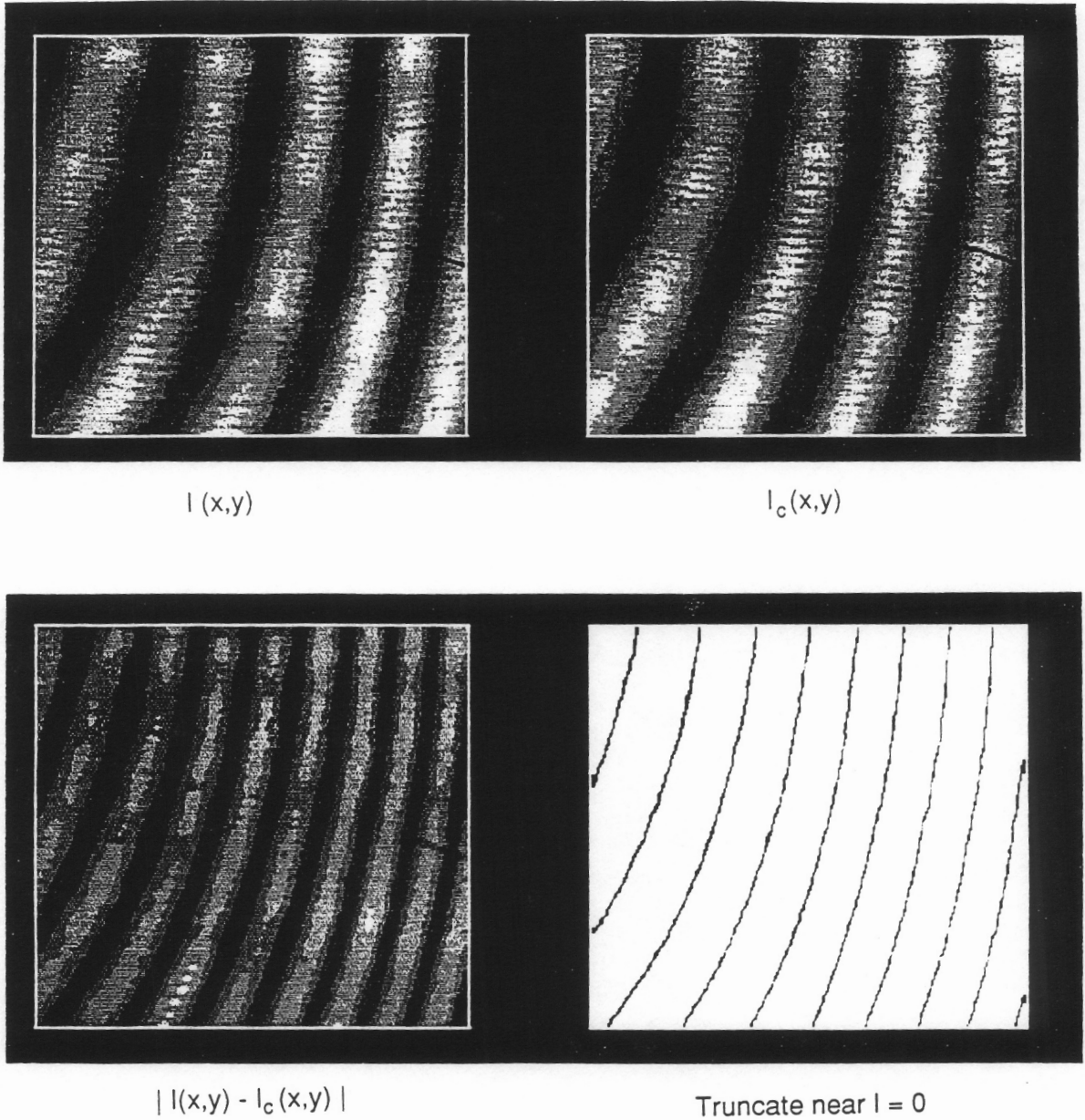


Fig. 20 Illustration of scheme 1 on a whole field base.

Now, let the intensities of the two beams that form the moire pattern vary from point-to-point in an arbitrary way expressed by  $I_1(x,y)$  and  $I_2(x,y)$ . The intensity of the moire pattern and its complement depend upon  $I_1(x,y)$ ,  $I_2(x,y)$  and their relative phase  $\phi(x,y)$  by

$$I(x,y) = I_1(x,y) + I_2(x,y) + 2\sqrt{I_1(x,y)I_2(x,y)}\cos\phi(x,y) \quad (22)$$

$$I_c(x,y) = I_1(x,y) + I_2(x,y) - 2\sqrt{I_1(x,y)I_2(x,y)}\cos\phi(x,y) \quad (23)$$

By subtraction,

$$I_r(x,y) = 4\sqrt{I_1(x,y)I_2(x,y)}\cos\phi(x,y) \quad (24)$$

which shows that the resulting intensity is a cosine curve modulated by a term containing the optical noise. The significant feature, however, is that  $I_r(x,y)$  is zero where  $\cos\phi$  is zero, independent of the noise function. If the points where the value of the cosine term is equal to zero are traced, the result is independent of the noise of the two input beams. The phase of these points can be expressed as

$$\phi(x,y) = N\pi + \frac{\pi}{2}, \quad N = 0, \pm 1, \pm 2 \dots \quad (25)$$

and these points correspond to those of fractional fringe orders of odd multiples of  $1/4$ , called quarter points.

Figure 21 illustrates how quarter points can be accurately determined without regard to the nonuniform illumination or the optical noise that is contained in the input beams. Figure 21(a) represents the moire pattern  $I$  and its complement  $I_c$ . The bold curve represents the scalar sum  $I_1+I_2$  as it appears in Eqs. (22) and (23). Its variation represents low frequency and high frequency noise. Although  $I_r$  (Eq. (24)) does not contain the term  $(I_1+I_2)$ , it still contains the noise information as a coefficient of the harmonic term. The noise might cause great distortions of the intensity distributions, but at the quarter points  $I(x,y) = I_c(x,y)$ . At quarter points, where  $\cos\phi(x,y) = 0$ , the three terms  $I$ ,  $I_c$  and  $(I_1+I_2)$  in Eqs. (22) and (23) all become equal as depicted in Fig. 21(a). Hence, after subtraction, the intensities at quarter points are zero, independent of noise (Fig. 21(b)). In Fig. 21(c), the negative portions of the curve are inverted by taking absolute values, providing sharp intensity minima at the quarter points. The quarter points are then located by truncating the curve near  $I = 0$ . Thus, the quarter points are located with high fidelity by a simple algorithm.

Fringe multiplication by an even multiplication factor  $\beta$  can be obtained from a series of moire patterns, each shifted by a constant phase of  $2\pi/\beta$ . These data are manipulated to produce a composite contour map. For example, to achieve  $\beta = 6$ , the series of patterns obtained with shifts of

$$\begin{array}{ccc} 0, & \pi/3, & 2\pi/3 \\ \pi, & 4\pi/3, & 5\pi/3 \end{array}$$

can be used, where each pattern has a phase difference of  $\pi/3$  with respect to the next pattern. Note that the shifted patterns in the bottom line are the complementary patterns of those in the top line. After subtraction of the complementary patterns, each of three images in the top line will produce two

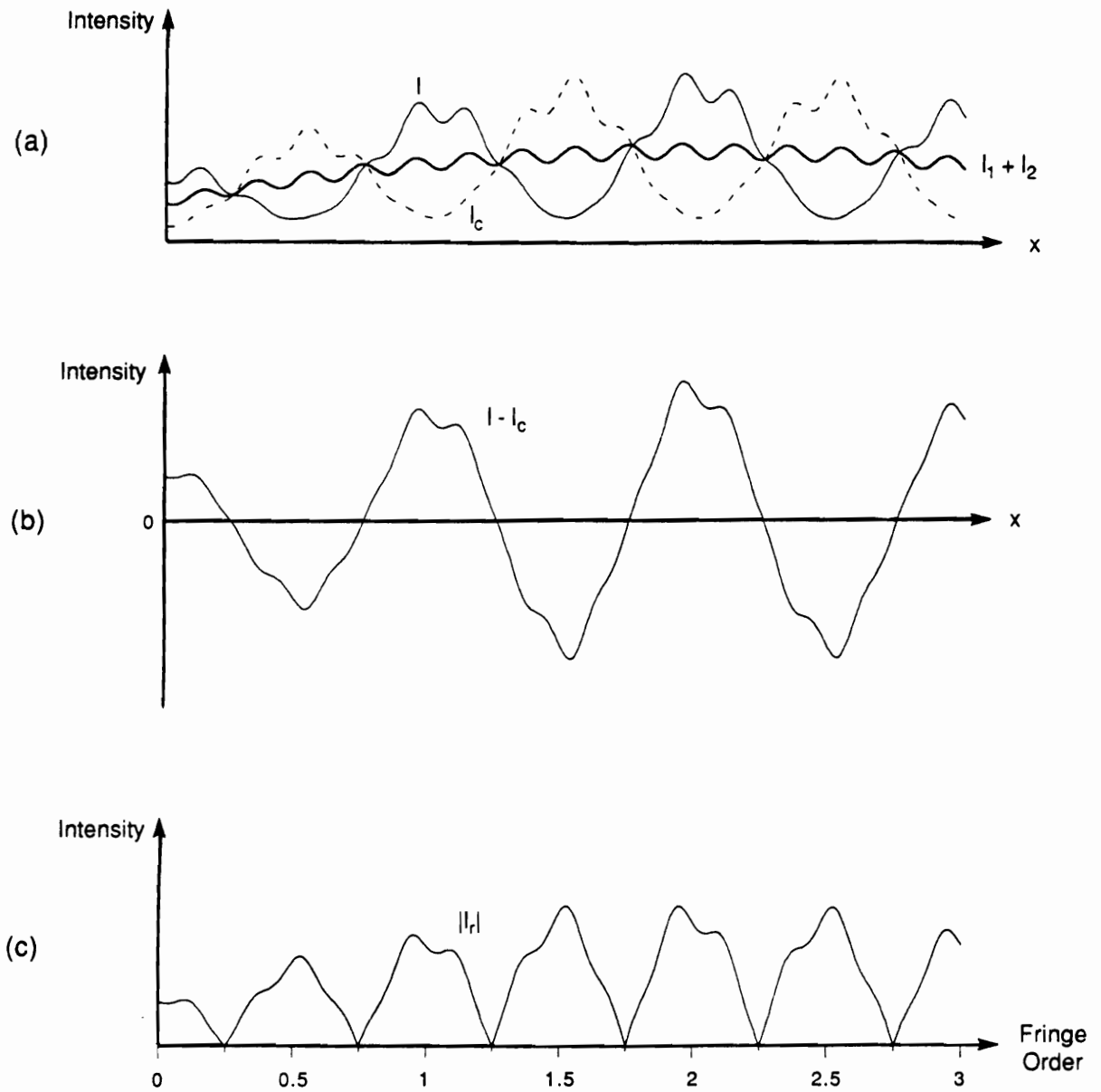


Fig. 21 Illustration of scheme 1 for the case of nonuniform illumination with optical noise.

quarter points, and thus six fringe contours will be formed for each fringe in the basic moire pattern  $I(x,y)$ . The six fringe contours will be separated by equal fringe order increments of  $1/6$ .

The result for the general case is a pattern of fringe contours of sensitivity  $g/\beta$  or  $1/\beta f$  per fringe contour. If fringe orders  $N^*$  are assigned to the combined pattern in the normal way and if rigid-body displacements are dismissed, the pattern represents a displacement field determined by

$$U = \frac{N^*}{\beta f} \quad (26)$$

where  $\beta$  is a fringe multiplication factor.

### 6.3 Scheme 2

With this scheme, a series of  $\beta$  fringe-shifted contours are obtained from  $\beta/2$  fringe-shifted moire patterns. Compared to scheme 1, only half as much experimental data are required.

Consider again a series of moire patterns that are fringe-shifted by a constant increment of  $2\pi/\beta'$ . Here,  $\beta' = \beta/2$ , or half the fringe multiplication factor. By recalling Eq. (22), the intensity distribution of these patterns can be expressed as

$$I_i(x,y) = I_1(x,y) + I_2(x,y) + 2\sqrt{I_1(x,y)I_2(x,y)} \cos\left(\phi(x,y) + \frac{2i\pi}{\beta'}\right) \quad (27)$$

$$i = 0, 1, \dots, \beta'-1$$

where  $I_i$  is the intensity distribution of the  $i^{\text{th}}$  shifted pattern, which is shifted by  $2i\pi/\beta'$  with respect to the original pattern. By subtracting the  $i^{\text{th}}$  shifted pattern from the  $j^{\text{th}}$  shifted pattern, one can obtain the resulting intensity distribution as

$$I_r(x,y) = I_j(x,y) - I_i(x,y) = 4\sqrt{I_1(x,y)I_2(x,y)} \sin\left(\phi(x,y) + \frac{(i+j)\pi}{\beta'}\right) \sin\left(\frac{(i-j)\pi}{\beta'}\right) \quad (28)$$

where  $i, j < \beta'$  and  $i \neq j$ .

Similar to Eq. (24), Eq. (28) clearly indicates that at the points where the phase  $\phi(x,y)$  satisfies the condition  $\sin\left(\phi(x,y) + \frac{(i+j)\pi}{\beta'}\right) = 0$ , the result will be independent of  $I_1$  or  $I_2$ . These phase values,  $\phi(x,y)$ , and the corresponding fractional fringe orders,  $N^*(x,y)$ , can be expressed as

$$\phi(x,y) = N\pi + \frac{(i+j)\pi}{\beta'} \quad (29)$$

$$N^*(x,y) = \frac{N}{2} + \frac{(i+j)}{2\beta'} \quad (30)$$

where  $N$  represents the fringe orders in the unshifted moire pattern.



As an example, consider the case of  $\beta' = 3$ . From the original ( $0^{\text{th}}$  shifted) pattern and the  $1^{\text{st}}$  shifted pattern, the values of  $\phi(x,y)$  between 0 and  $2\pi$  that satisfy Eq. (29) are  $\pi/3$  and  $4\pi/3$ . These correspond to fractional fringe orders  $1/6$  and  $4/6$ . Table 4 shows the phase  $\phi(x,y)$  and the corresponding fractional fringe orders for all three possible combinations of the shifted patterns. If three pairs are combined in a single pattern, the result is 6 times as many fringes as are present in each shifted pattern. That is, in this scheme, the sensitivity can be increased by a factor of  $2\beta'$ . This is equivalent to the case of scheme 1 with  $\beta = 6$ .

Figure 22 illustrates how the effects of noise are canceled by this scheme for the above case. Figure 22(a) illustrates the intensity distributions of three shifted patterns, where the input intensity variations are nonuniform; for the purpose of illustration, however, the nonuniformity or noise is less severe than that shown in Fig. 21. The uppermost curve shown here as an envelope, represents the intensity distribution when constructive interference occurs everywhere in the field. This intensity, which includes the noise, can be considered invariant. It is modulated at each point in proportion to the idealized intensity distribution of a moire pattern. Accordingly, the noise also appears in the original and the two shifted patterns (Fig. 22(a)), but attenuated in proportion to the intensity levels in the idealized moire pattern. Consequently, the attenuation of noise is identical wherever  $I_i = I_j$ , and unequal elsewhere. The noise does not influence the locations of the points of intersection of these curves. Hence, after subtraction, the curves of Fig. 22(b) cross the zero-intensity axis at the correct point, independent of optical noise. These crossings

Table 4. Phase values and fringe orders for an example of scheme 2.

Pair of Images	Phase ( Fringe Order )	
	$N = 0^\dagger$	$N = 1^\dagger$
0 <sup>th</sup> pattern 1 <sup>st</sup> pattern	$\pi/3$ ( 1/6 )	$4\pi/3$ ( 2/3 )
1 <sup>st</sup> pattern 2 <sup>nd</sup> pattern	$\pi$ ( 1/2 )	$2\pi$ ( 1 )
0 <sup>th</sup> pattern 2 <sup>nd</sup> pattern	$2\pi/3$ ( 1/3 )	$5\pi/3$ ( 5/6 )

<sup>†</sup> Values in Eqs. 29, 30

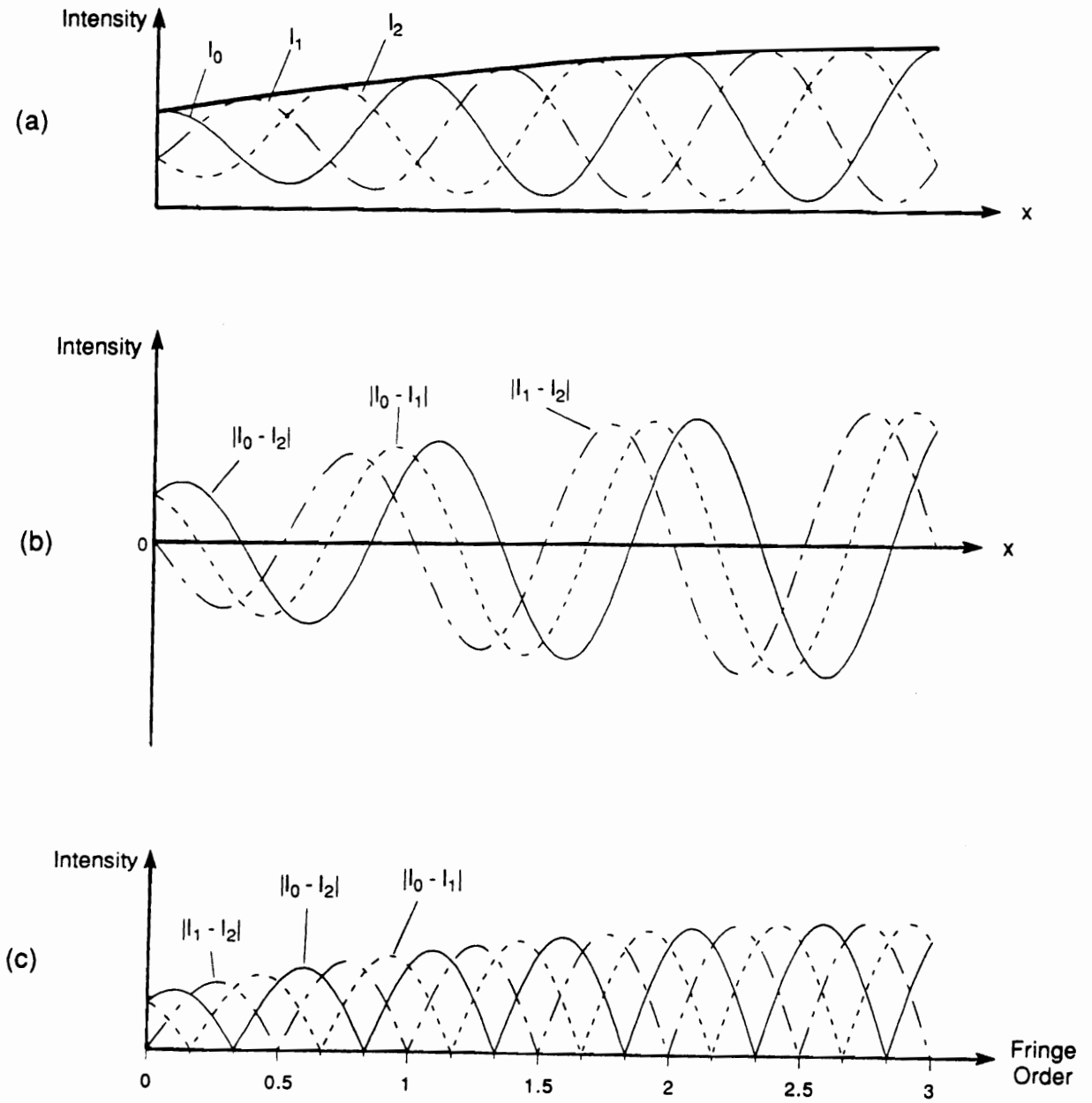


Fig. 22 Illustration of scheme 2 for the case of nonuniform illumination.

are points of fractional fringe orders of multiples of  $1/6$ . In Fig. 22(c), the negative portions of the curve are inverted by taking absolute values like in scheme 1. This provides sharp intensity minima at those points.

The idea of subtraction was suggested personally by K-S Kim and it can be found in [55]. The algorithms employed here to locate fringe positions after subtraction are less complicated than those of [55] and only one pair of images was utilized in [55] whereas a series of shifted images was introduced here to produce multiplication of fringe contours. In addition, the enhancement of the sensitivity by another factor of 2 in scheme 2 was also introduced here.

Scheme 2 has the advantage that fewer experimental data are required. Scheme 1 has the advantage that data are taken at the quarter points, where the gradient of intensity vs. fringe order is greatest. In the example, data at the  $N/6$  points were used, where intensity gradients remain strong (Fig. 22(a)) and the crossing points remain well defined.

## 6.4 Combination of Fringe-shifted Patterns

For the applications of current importance, the enhancement of the sensitivity provided by scheme 2 was not needed. Thus, scheme 1 was used to sharpen the fringes. In this case, only quarter points of all shifted images appeared in the composite fringe contour map. Random noise such as electrical noise and noise due to the imperfection of the specimen grating was eliminated most effectively at the quarter points because the slope of the

intensity distribution has its maximum value at the points, or in other words, the intensity varies most rapidly at these points. A low pass filter used to minimize the random noise was a 3x3 or 5x5 convolution with center pixel weight of 1.

The final step requires the superposition of fringe contours obtained from each pair of shifted moire patterns. A computer program to obtain the composite fringe contour map was written in C Language (Microsoft C Compiler Version 6.0) according to the flow chart shown in Fig. 23. First, a series of fringe-shifted patterns were retrieved and subtraction was done for each of the  $\pi$ -shifted pairs. Next, the low pass filtering process was performed on each of those images. The resulting images were binarized with a threshold value near zero grey level. This produced contour lines which represented the fringes. The final step after all the contour lines were obtained, was to assemble them to form a composite contour map. Of course, the composite map had  $\beta$  times as many contour lines as were present in each individual moire pattern. Hence the sensitivity was increased by the same factor which corresponds to the fringe multiplication factor  $\beta$ .

A CCD video camera (Model XC-77 by SONY) was used to capture the fringe patterns. It was connected to a frame grabber (Silicon Video Mux by EPIX) which converted the analogue image to digital arrays, and thus allowed the images to be stored and manipulated digitally by a computer. The frame grabber stored each video frame as a 480 x 480 array of 8 bit (256) grey levels for a total storage requirement of approximately 230K bytes per frame. Image processing was carried out through a personal computer (IBM PS2, Model 80) and the result was printed by a laser printer.

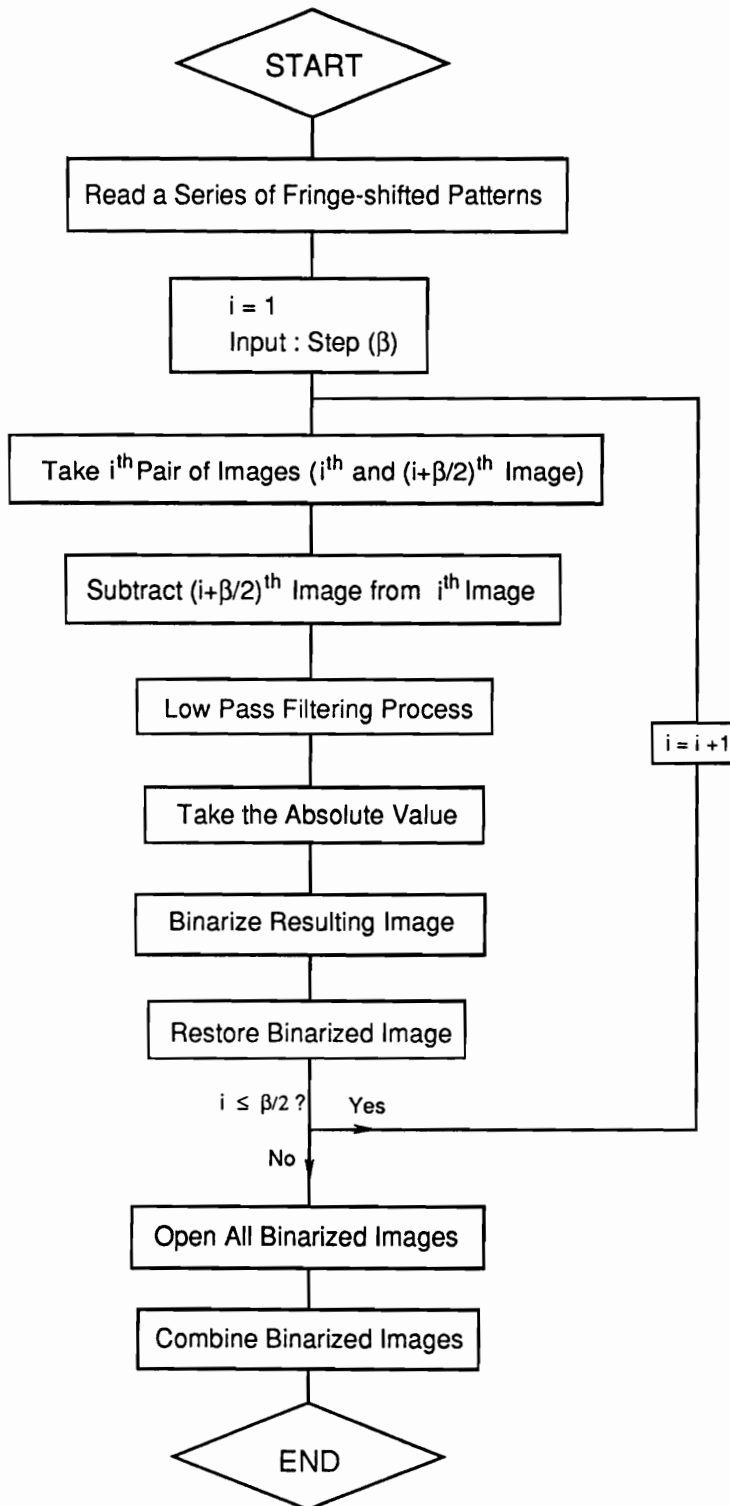


Fig. 23 A flow chart for obtaining the composite contour map.

## 7.0 DEMONSTRATIONS

### 7.1 Normal Strains across an Interface in a Thick Graphite/Epoxy Composite

Micromechanical behavior at the 0/90° interface of a thick, cross-ply graphite/epoxy composite laminate was investigated. The specimen was loaded in interlaminar compression and the deformation normal to the ply interface was documented.

The specimen was cut from a thick-walled cylinder with outside diameter of 203mm (8 in.). The specimen is illustrated and described in Fig. 24. The xyz coordinates correspond to the radial, axial and hoop directions of the cylinder, respectively. The specimen ends were ground flat and blocks of the same material were attached by a cyanoacrylate adhesive to extend the specimen height. This was done to minimize the influence of friction forces generated between the loading platens and the composite specimen. The specimen grating was replicated on face A (the xy plane) and the specimen was loaded in a stiff loading frame that was mounted on the heavy-duty rotary stage to control in-plane rigid-body rotation of the specimen.

Figure 25 depicts the longitudinal or V displacement field on Face A with a sensitivity of 104nm per fringe contour ( $\beta = 2$ ). The fringe gradient (normal strain  $\epsilon_y$ ) is greater in the 90° ply than the 0° ply. This is made clearer in Fig. 26, where the fringe pattern is transformed by carrier fringes of rotation such that the

**Graphite/Epoxy**  
Stacking Sequence:  $[90_4/0_2]_n$   
Material System: IM6/2258  
Ply Thickness: 0.19 mm (0.075 in.)

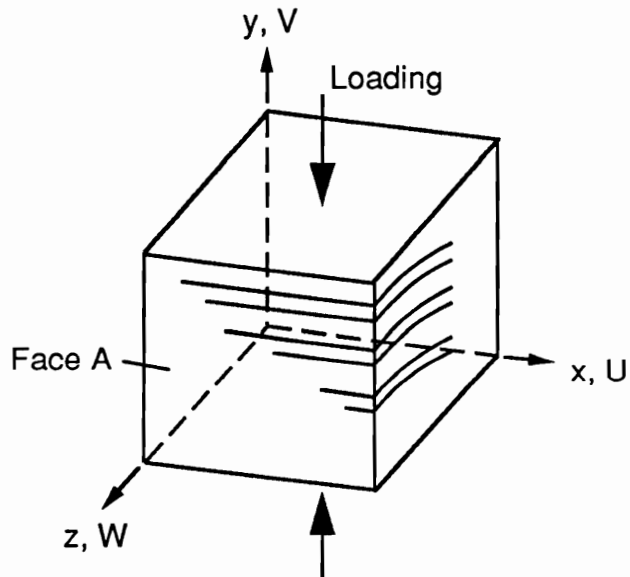


Fig. 24 The graphite/epoxy composite specimen.



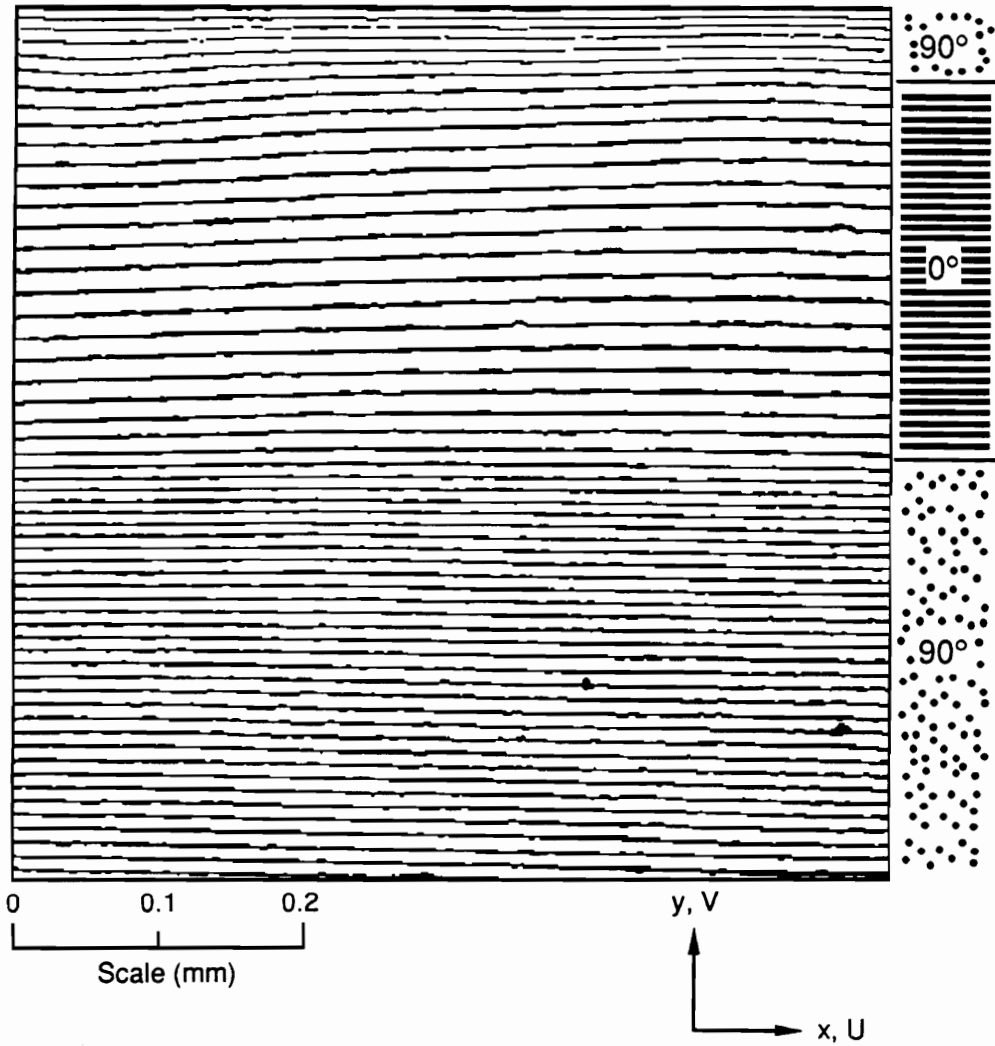


Fig. 25  $N_y^*$  field near  $0/90^\circ$  interfaces. Sensitivity is 104nm per fringe contour.

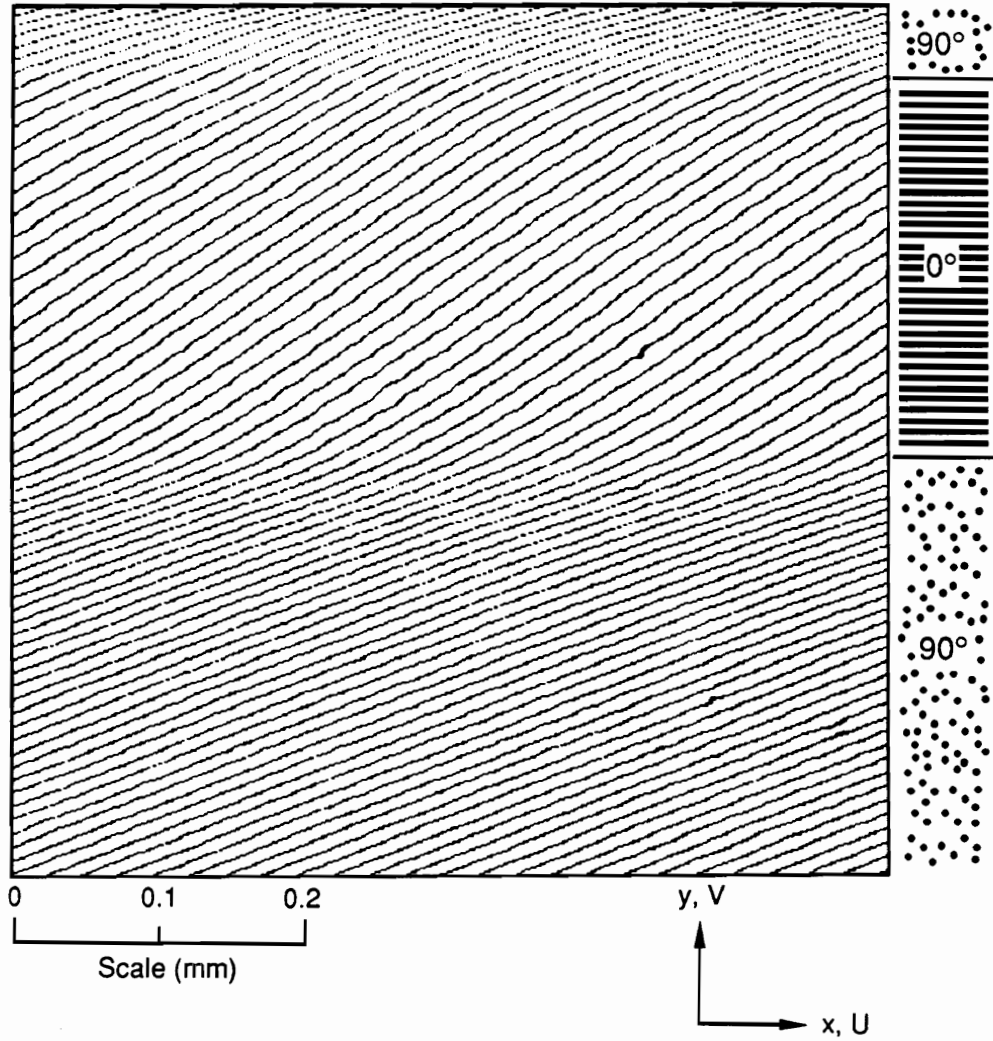


Fig. 26  $N_y^*$  field with carrier fringes of rotation.  
Sensitivity is 104nm per fringe contour.

slope of a fringe at any point is inversely proportional to the normal strain  $\varepsilon_y$  at the point [28]. This behavior was ascribed to the free surface effect of composites wherein constraints that exist in the interior of a body vanish or relax at free surfaces.

In order to emphasize this state of strain along the  $0^\circ/90^\circ$  ply interface, the carrier fringe technique was used to transform the displacement field into that illustrated in Fig. 27. Here, a uniform normal strain was subtracted by carrier fringes of extension so that the sign of the fringe gradient at the  $0^\circ$  ply becomes opposite to that at the  $90^\circ$  ply; in addition, carrier fringes of rotation were used to obtain continuous fringes across the interface. Again the slope of the fringes relates to the strain  $\varepsilon_y$ . The extremely large change near the interface indicates a severe  $\varepsilon_y$  strain gradient.

Note that subtraction of the uniform part of the displacement field transformed the fringe pattern to a very sparse pattern, with few fringe contours. Accordingly, a higher sensitivity was required to document the displacement field after subtraction by carrier fringes of extension. In Fig. 27, the sensitivity was increased by another factor of 4 compared to that used in Fig. 25 and 26. The fringe multiplication factor is  $\beta = 8$  and the sensitivity is 26nm per fringe contour.

Figure 28 illustrates the same type of displacement field but documented in a different location. The pattern shows stronger strain gradients at the ply interface. This variation is a consequence of inherent variability in composite materials. Material variability includes the variation of thickness of the resin rich

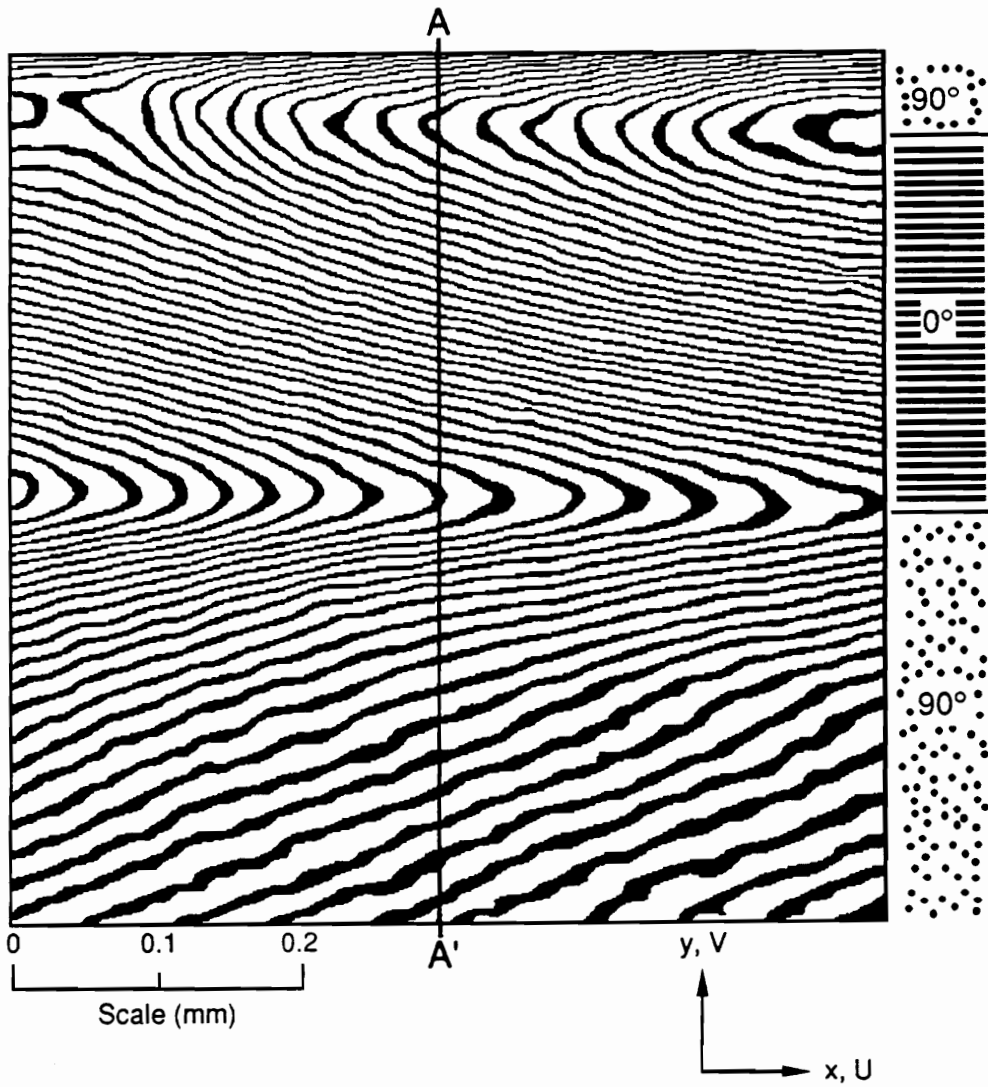


Fig. 27  $N_y'$  field with carrier fringes of rotation and extension.  
Sensitivity is 26nm per fringe contour.

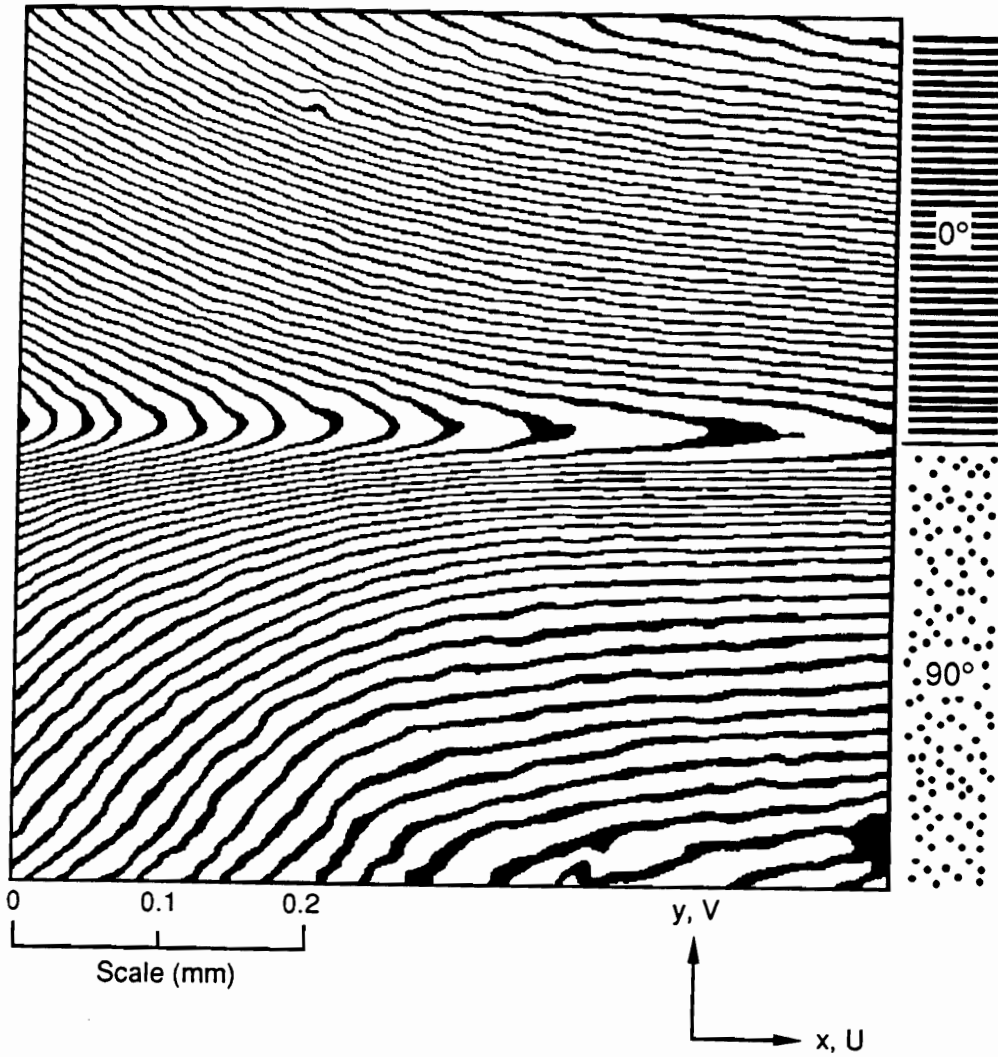


Fig. 28  $N_y^*$  field with carrier fringes of rotation and extension, documented in a different location. Sensitivity is 26nm per fringe contour.

zone near ply interfaces, which appears as a critical parameter of the local deformation.

The strain distribution along A-A' (Fig. 27) was determined and it is plotted in Fig. 29. The normal strains  $\epsilon_y$  in each ply become increasingly dissimilar as they approach the interface, but then the curves turn around and join. The result is a very large  $\epsilon_y$  strain gradient near the interface. A similar distribution was obtained in a related experimental study of a bimaterial joint [56] where steel and brass plates were joined along a flat interface by silver solder.

## 7.2 Deformation of Metal/Matrix Composites

Deformation of metal/matrix composites is demonstrated for two different materials: a unidirectionally reinforced boron/aluminum composite and a siliconcarbide/aluminum composite with a stacking sequence of  $[90/0]_{2s}$ . Specimens were prepared so that  $0^\circ$  fibers were perpendicular to the cross section. Specimen gratings were replicated on the face illustrated in Fig. 30 and the specimens were loaded in compression.

The boron/aluminum specimen was tested within the elastic range. The V displacement field is illustrated in Fig. 31 where  $\beta = 8$  and a sensitivity of 26nm per fringe contour was used. The approximate centers of the fibers are marked with an asterisk. The phenomenological behavior is evident, wherein large differences of deformations are found on a fiber-by-fiber basis, and

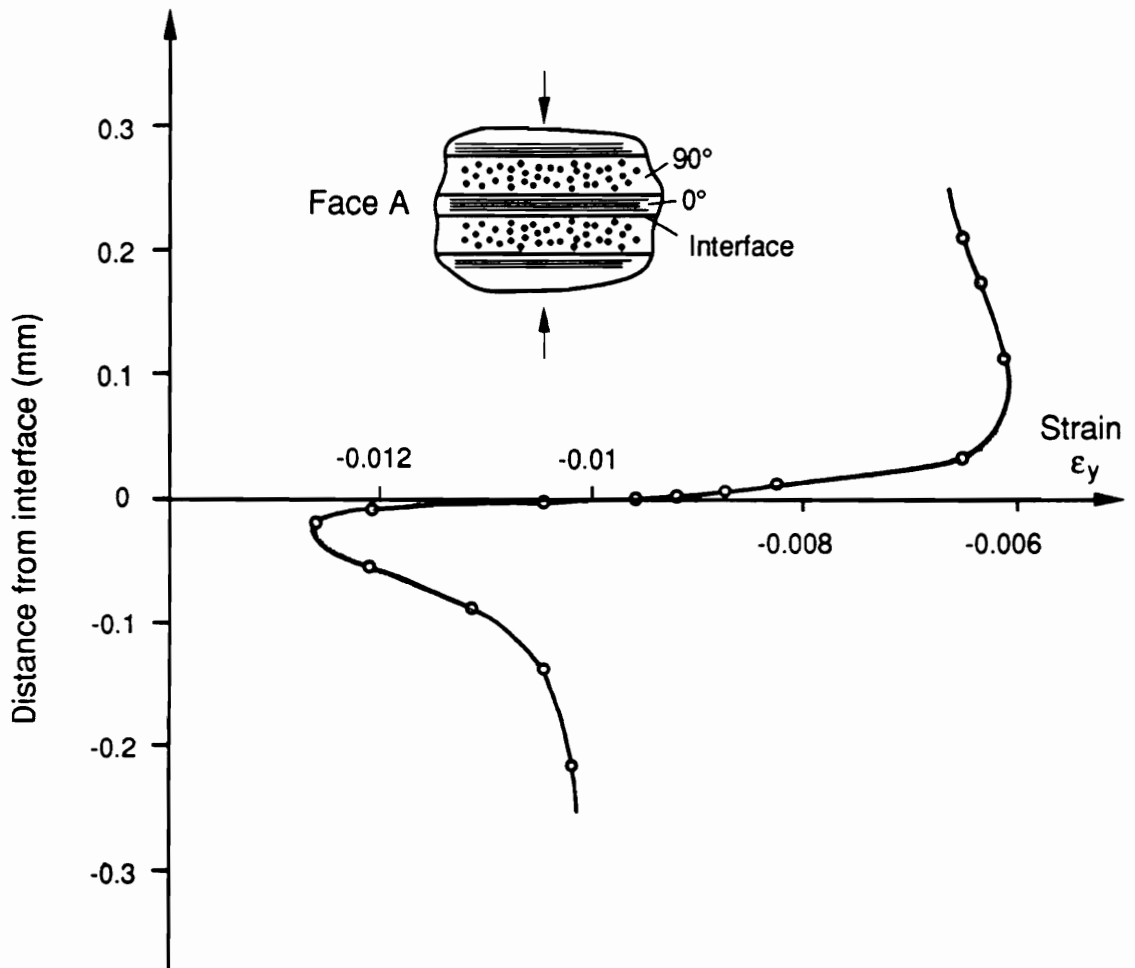


Fig. 29 Strain distribution across the interface.

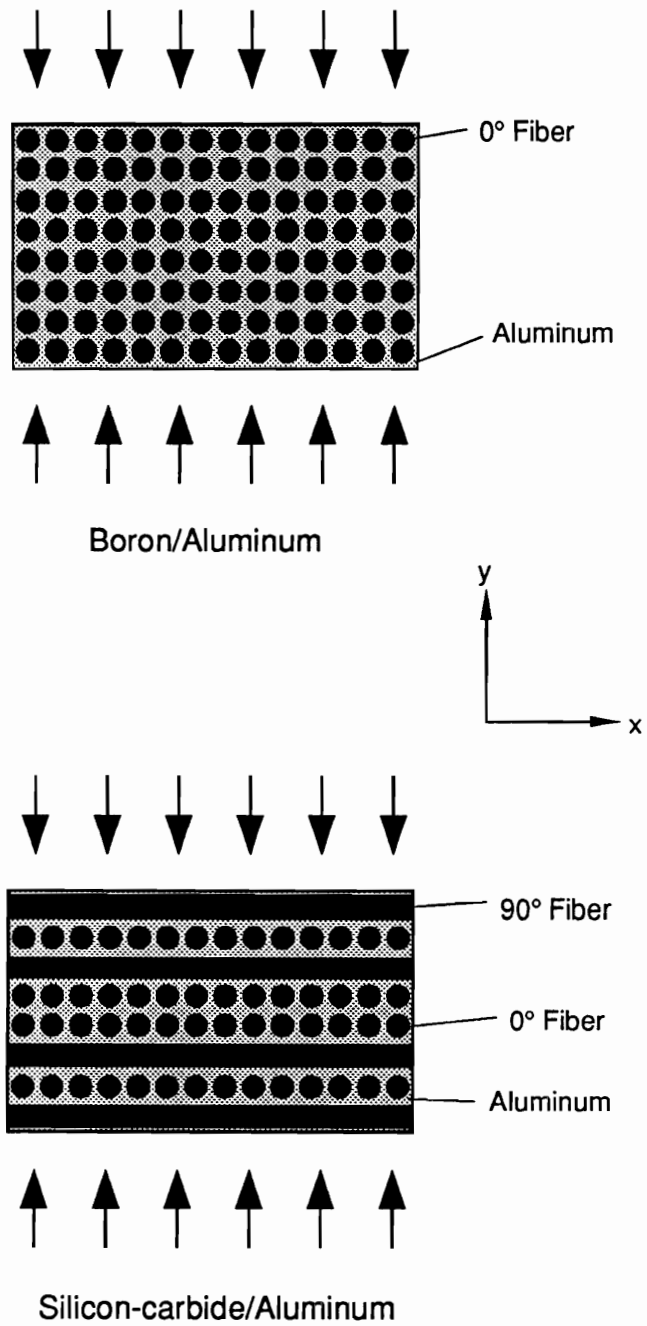


Fig. 30 The metal/matrix specimens.



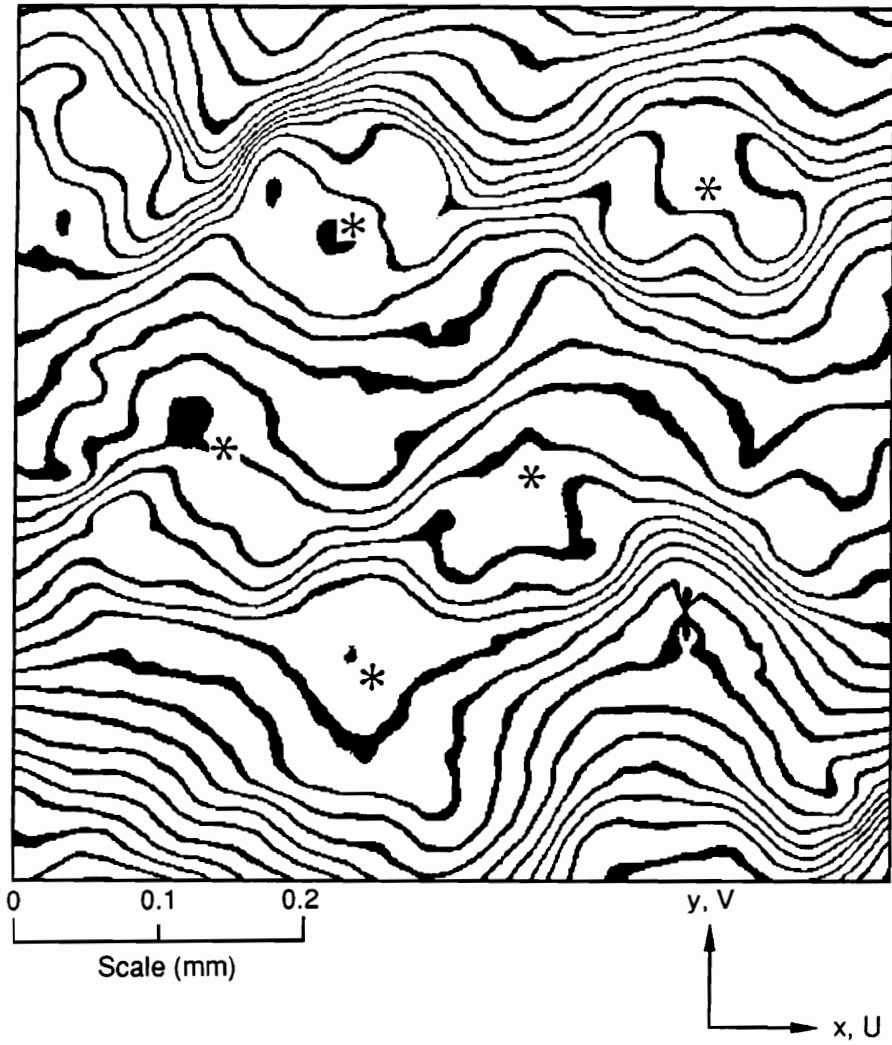


Fig. 31  $N_y$  field of the boron/aluminum specimen. Sensitivity is 26nm per fringe contour.

presumed symmetries and regularities are absent. Strain concentrations are evident near several fiber/matrix interfaces.

The silicon-carbide/aluminum specimen was subjected to a higher load, which incurred plastic deformations in the ductile aluminum matrix. A fringe pattern depicting the  $V$  displacement field is shown in Fig. 32 where a sensitivity of 52nm per fringe contour was used. Significant strain concentrations are observed near all fiber/matrix interfaces. Figure 33 shows the corresponding  $U$  displacement field.

A higher load was applied to the specimen and the two  $0^\circ$  plies at the center of the specimen (region marked by a box in Fig. 32) were observed with a higher magnification. Figure 34 depicts the  $V$  displacement field with carrier fringes of extension. The carrier fringes were used to cancel the fringes corresponding to the normal strain  $\epsilon_y$  of the fibers to document the relative deformation between fiber and matrix.

### **7.3 Thermal Deformation of a Microelectronic Assembly**

The solder ball interconnection is widely used for a computer chip to ceramic substrate assembly. In the technique, solder balls are used between the chip and ceramic substrate as illustrated in Fig. 35 and the assembly is then subjected to thermal cycles in the application. A thermal expansion mismatch between the chip and ceramic substrate is a critical design parameter because it creates deformations and stresses at each solder joint, and causes electrical

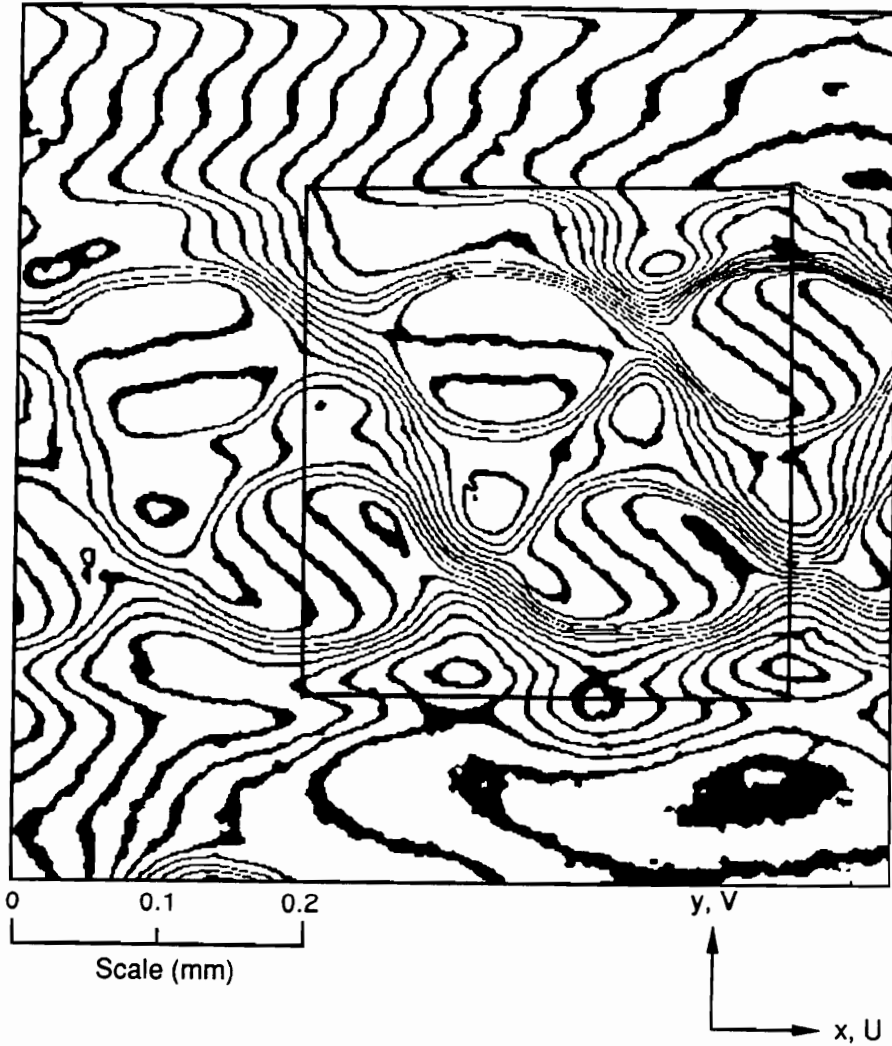


Fig. 32  $N_y$  field of the silicon-carbide/aluminum specimen.  
Sensitivity is 52nm per fringe contour.

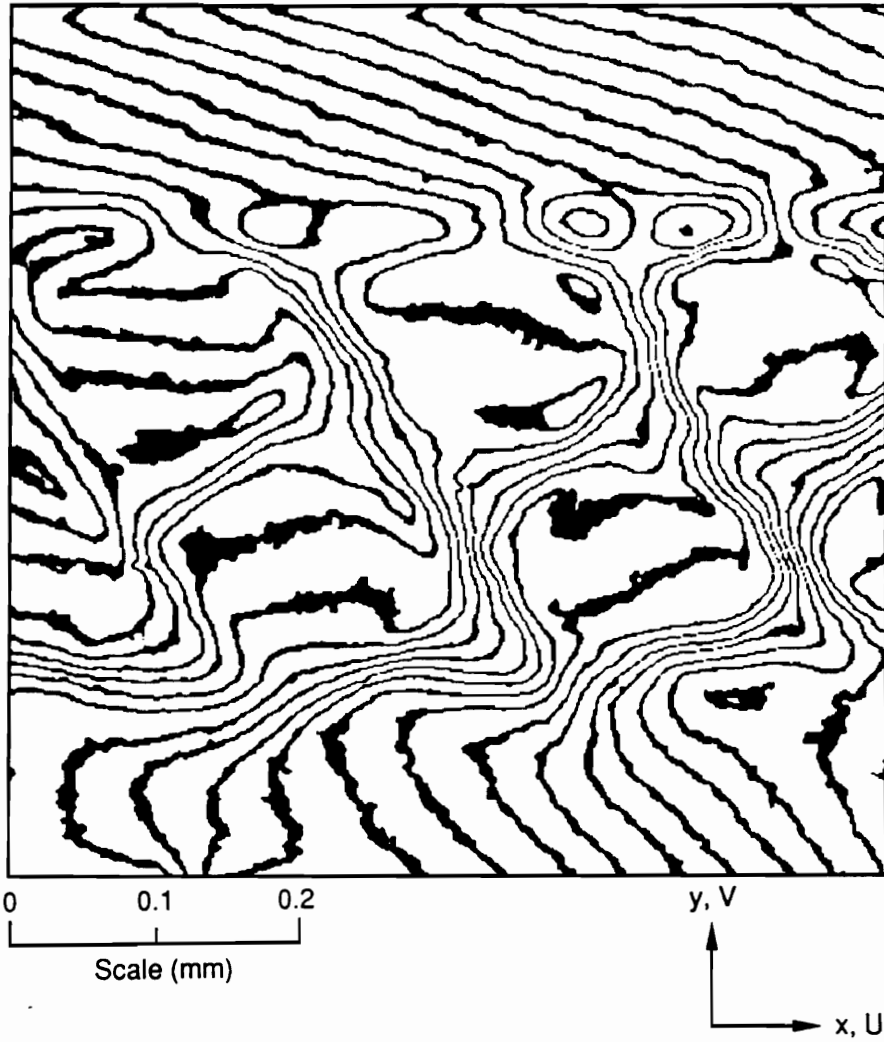


Fig. 33  $N_x$  field of the silicon-carbide/aluminum specimen.  
Sensitivity is 52nm per fringe contour.

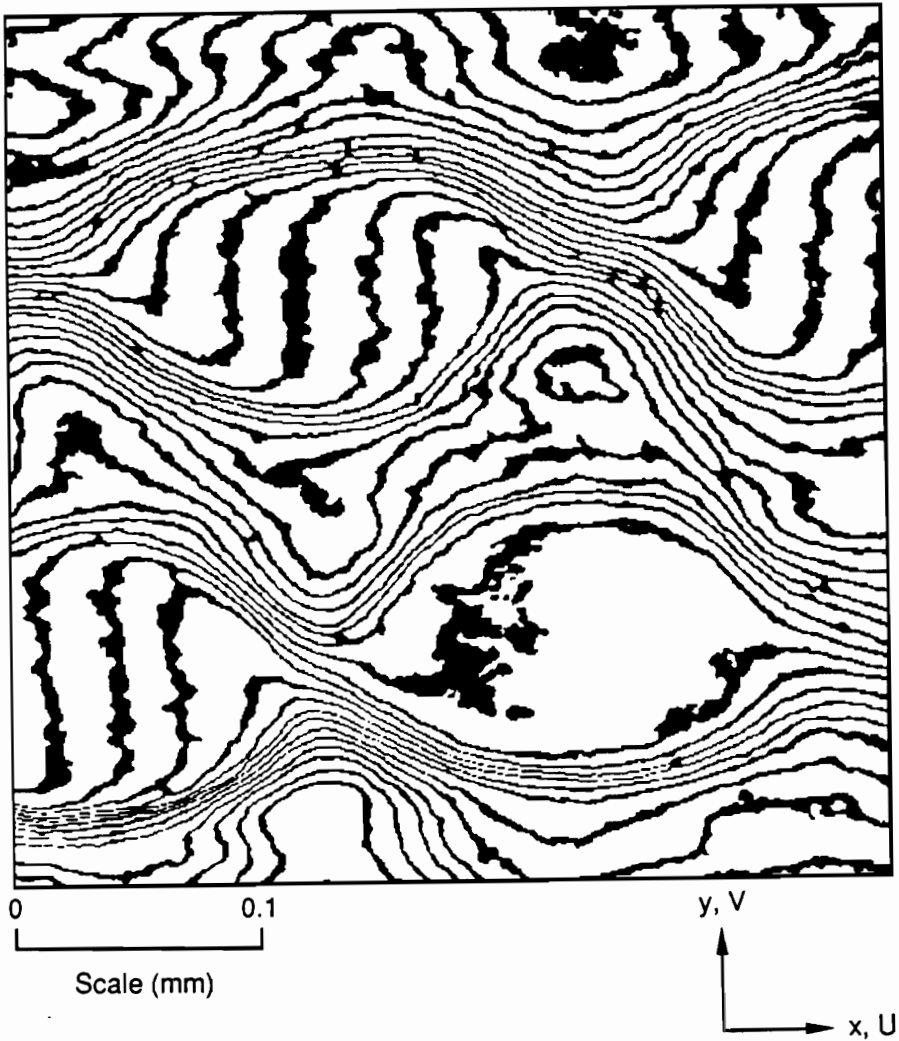


Fig. 34  $N_y$  field of the silicon-carbide/aluminum specimen with carrier fringes of extension for a higher load. Sensitivity is 52nm per fringe contour.

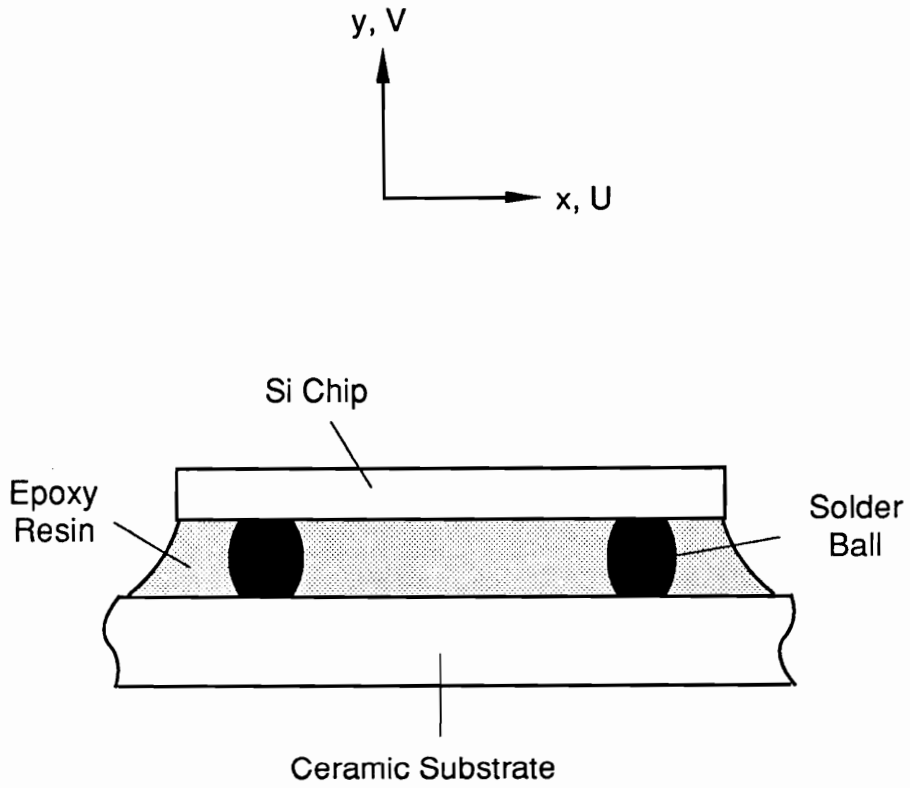


Fig. 35 Illustration of the solder ball interconnection technique.

and mechanical failures. An epoxy resin with coefficient of thermal expansion similar to that of solder can be used to improve the condition by reducing thermal strains in the solder balls. The strain distributions of this type of package was measured, especially around the solder joints embedded in the epoxy encapsulant.

The experimental procedure for determination of steady state thermal strains by moire interferometry is reported in [57]. Briefly, a special grating mold is produced on a zero-expansion substrate so that it has the same frequency at room temperature and elevated temperature. This mold is used to replicate a specimen grating at elevated temperature. It is also used to adjust the frequency of the virtual reference grating at room temperature. Then, the deformation of the specimen and specimen grating is observed at room temperature. Thus, the absolute change of specimen grating frequency, induced by cooling the specimen, is recorded in the moire pattern.

The V and U displacements are depicted in Figs. 36 and 37, respectively, where  $\Delta T$  of  $62^\circ\text{C}$  was used. The sensitivity used here was 17nm per fringe contour, which corresponds to a fringe multiplication  $\beta$  of 12. While the location of the solder ball is evident in both fields, the presence of the epoxy encapsulant eliminates the serious strain concentrations that would otherwise occur at the solder joint. In Fig. 36, the closely spaced fringes in the epoxy resin represent the thermal expansion of the epoxy and solder ball normal to the chip surface, but the corresponding thermal expansion parallel to the chip (Fig. 37) is restrained by the mating parts. Only tiny shears are developed. The normal stresses  $\sigma_x$  and  $\sigma_y$  in any material depend upon the strain parameter:

measured strain minus that from free thermal expansion in the respective materials.



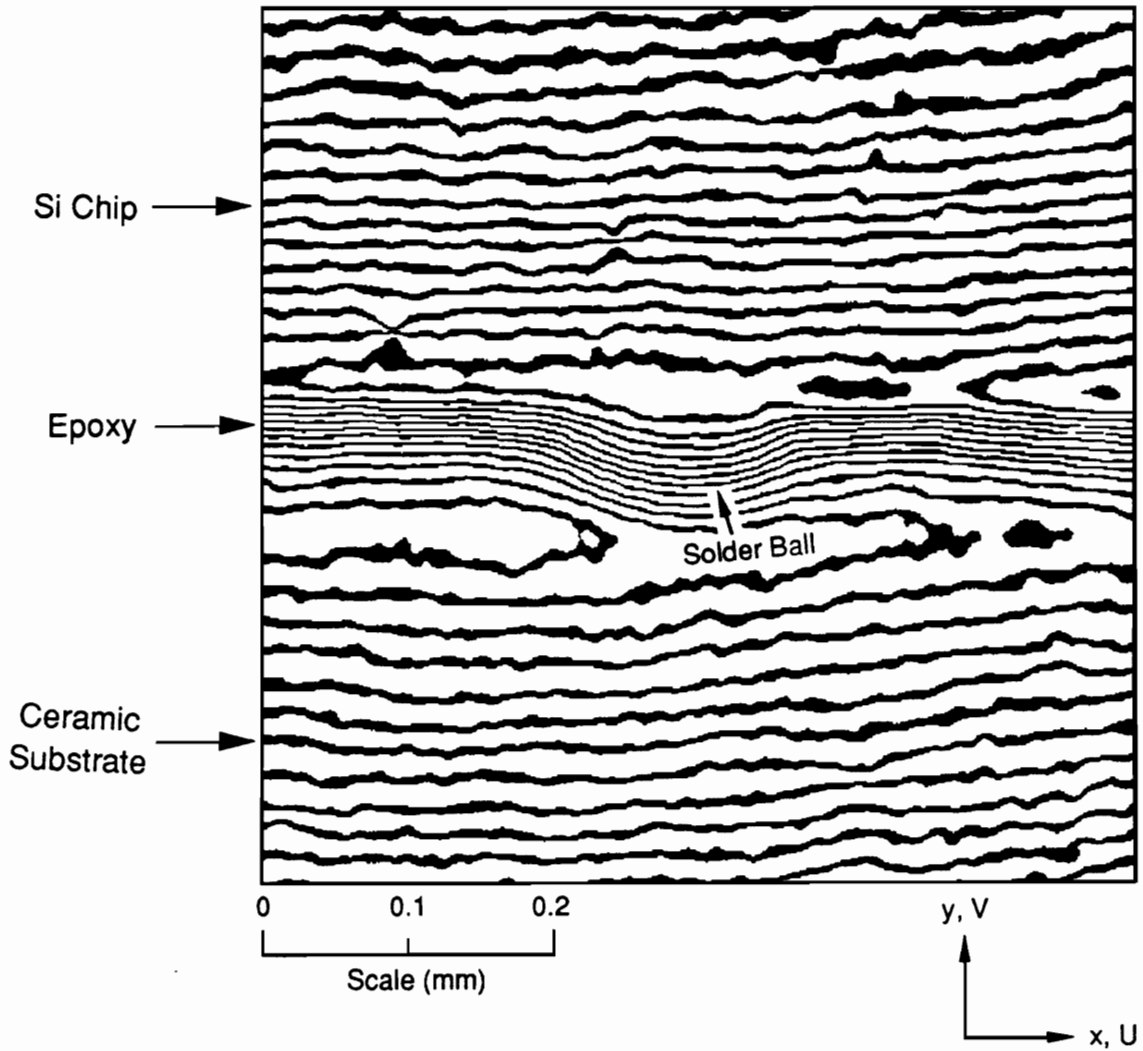


Fig. 36  $N_y^*$  field around a solder joint. Sensitivity is 17nm per fringe contour.

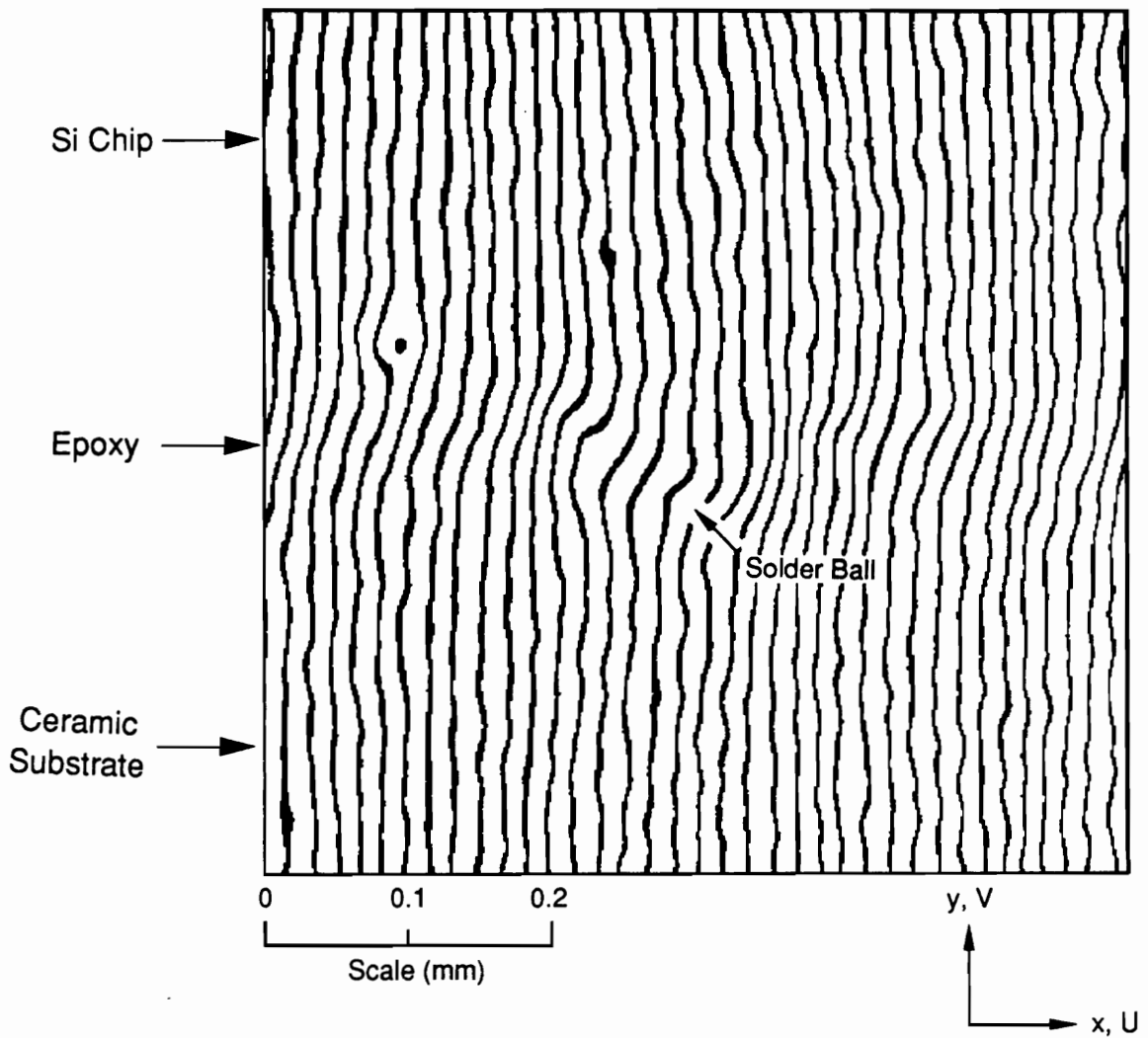


Fig. 37  $N_x^*$  field around a solder joint. Sensitivity is 17nm per fringe contour.

## **8.0 DISCUSSION AND FUTURE WORK**

### **8.1 Further Enhancement of the Sensitivity of Moire Interferometry**

In this work, BK7 was used as a refractive medium to produce a basic sensitivity of 208nm per fringe order. The basic sensitivity can be further increased by using other refractive media introduced in Chap. 2. All the optical glasses seem to be practical. When LaSF6 is used with a visible green light ( $\lambda = 514\text{nm}$ ), a sensitivity of 144nm per fringe order can be achieved, which, combined with a fringe multiplication factor of 12, will produce a final sensitivity of 12nm per fringe contour. An optical crystal can be used for a still further increase of the sensitivity.

An antireflection coating was not applied to the top surface of the immersion interferometer. This resulted in a ghost pattern but its influence was minor because reflectance at the BK7/air interface was very small. If optical glasses with higher refractive index are used, an antireflection coating must be applied to the top surface of the immersion interferometer. Note that the fringe processing scheme nullifies the influence of optical noise in the incident beams, but it does not treat all the noise introduced in the optical system after the moire pattern is formed.

## 8.2 Specimen Grating

In this work, second-order diffraction beams were used together with a specimen grating of 1200 lines per mm to create a virtual reference grating of 4800 lines per mm. To accommodate the current enhanced sensitivity of moire interferometry, specimen gratings of 2400 lines per mm would allow use of the first-order diffraction, thus increasing diffraction efficiency and reducing noise. Accordingly, the production of higher frequency specimen gratings should be undertaken to complement the immersion interferometer.

Photoresist gratings of a frequency as high as 4400 lines per mm could be produced in air with visible light. Higher frequency could be produced, too, if the grating is made in a refractive medium.

Another factor relating to practical application of the method to micromechanics is the thickness of the specimen grating. For macromechanics, the usual replication technique produces a grating thickness of about 25  $\mu\text{m}$ . For the small fields of micromechanics, this can be reduced to about 5  $\mu\text{m}$ . Whereas the deformation of the specimen surface is sought, the deformation on the outside surface of the grating is actually observed and measured. The difference is negligible for most problems, but in some micromechanics studies, where strain gradients are very large, it could be significant. Shear lag through the thickness of the grating could mask the true displacement behavior in zones of abrupt changes or discontinuities of displacements.

Two levels of improvement are available to nullify the shear lag. Instead of applying the specimen grating by replication, gratings can be produced

directly on the specimen surface in submicron thickness by using photoresist; this seems very practical for the small fields of view encountered in micromechanics. Beyond this, a specimen grating of zero thickness can be produced on metals, ceramics and other materials by plasma etching, using a photoresist grating as a mask [58].

## 9.0 CONCLUSIONS

An ultra-high sensitivity whole-field in-plane displacement measurement technique was developed for micromechanics. The development included enhancement of the basic sensitivity of moire interferometry beyond the previously conceived theoretical limit and development of an automatic fringe shifting and fringe sharpening scheme for fringe multiplication.

With the enhanced basic sensitivity of 208nm per fringe order, a sensitivity of 17nm per fringe contour was achieved by fringe multiplication of 12; this sensitivity corresponds to that of moire with 57,600 lines per mm (1,463,000 lines per in.). A spatial resolution of 2-5 $\mu$ m and a large dynamic range in deformation measurements of 0-10% were also achieved.

The technique was demonstrated for diverse micromechanical problems of current importance. The development is ideally suited for the study of a broad range of problems in micromechanics, providing an extremely robust system for ultra-high sensitivity of deformation measurements.

## 10.0 REFERENCES

1. Post, D., Guo, Y. and Czarnek, R, "Deformation Analysis of Boron/ Aluminum Specimens by Moire Interferometry," *Metal Matrix Composites: Testing, Analysis, and Failure Modes, ASTM STP 1032*, W. S. Johnson, Ed., Am. Soc. Test. Mat., Philadelphia, 1989.
2. Post, D., Dai, F. L., Guo, Y. and Ifju, P., "Interlaminar Shear Moduli of Cross-Ply Laminates: An experimental Analysis," *Journal of Composite Materials*, pp. 264-279, March 1989.
3. Fourney, M. E., Gao, Q. Y. and Wiberg, E., "Micromechanical Strain Measurement Near a Crack Tip in 2091 AL-Li Alloy," *Micromechanics: Experimental Techniques*, W. N. Sharpe, Jr., Ed., ASME, NY, pp. 101-104, Dec.1989.
4. Mao, T. H., Beaumont, D. W. R. and Nixon, W. C., "Direct Observation of Crack Propagation in Brittle Materials," *J. Mat. Sci. Lett.*, vol. 2, pp. 613-616, 1983.
5. Davidson, D. L. and Lankford, J., "Dynamic, Real-Time Fatigue Crack Propagation at High Resolution as Observed in the Scanning Electron Microscope," ASTM STP 675, *Am. Soc. Test. Mat.*, Philadelphia, pp. 277-284, 1978.
6. Davidson, D. L., "The Observation and Measurement of Displacements and Strains by Stereoimaging," *Scanning Electron Microscopy/1979/II*, SEM Inc., AMF O'Hare, IL., pp 79-86, 1979.
7. Kurtschot, M. T., "High Resolution Strain Measurement by Direct Observation in SEM," *J. Mater. Sci.*, 23, pp. 3970-3972, 1988.

8. Daniel, I. M., Anastassopoulos, G. and Lee, J.-W., "Experimental Micromechanics of Brittle-Matrix Composites," *Micromechanics: Experimental Techniques*, W. N. Sharpe, Jr., Ed., ASME, NY, pp. 133-146, Dec.1989.
9. Zehnder, A. T. and Rosakis, A. J., "Temperature Fields Generated During Dynamic Crack Growth in Metals: High Resolution Measurements by Means of High Speed Infrared Detectors," *Micromechanics: Experimental Techniques*, W. N. Sharpe, Jr., Ed., ASME, NY, pp. 33-54, Dec.1989.
10. Hartley, K. A., Duffy, J. and Hawley, R. H., "Measurements of the Temperature During Shear Band Formation in Steels Deforming at High Strain Rates," *J. Mech. Phys. Solids*, vol. 35, pp. 283-301, 1987.
11. Brennan, J. J., and Prewo, K. M., " Silicon Carbide Fiber Reinforced Glass-Ceramic Matrix Composites Exhibiting High Strength and Toughness," *J. of Material s Science*, vol. 17, pp. 2371-2383, 1982.
12. Marshall, D. B. and Evans, A. G., "Failure Mechanisms in Ceramic-Fiber/Ceramic-Matrix Composites," *J. of the Amer. Ceramic Soc.*, vol. 68, pp. 225-231, 1985.
13. Post, D., "Optical Interference for Deformation Measurement -- Classical Holographic and Moire Interferometry," *Mechanics of Non-Destructive Testing*, W. W. Stinchcomb, Ed., Plenum Press, NY, pp. 1-53 ,1980.
14. Post, D. and W. A. Baracat, "High-Sensitivity Moire Interferometry -- A simplified approach," *Experimental Mechanics*, vol. 21, no. 3, pp. 100-104, 1981.
15. Post, D., "Developments in Moire Interferometry," *Opt. Eng.*, 21, no. 3, pp. 458-467, May 1982.



16. Mckelvie, J. and Walker, C. A., "A Practical Multiplied Moire-fringe Technique," *Experimental Mechanics*, vol. 18, no. 8, 1978.
17. Parks, V. J., "Geometric Moire," *Handbook on Experimental Mechanics*, A. S. Kobayashi, Ed., Prentice-Hall, Englewood Cliffs, NJ, 1987.
18. Shield, T. W., Kim, K.-S. and Nikolic, R., "Moire Microscope for the Experimental Determination of the In-Plane Displacement Near a crack Tip in a Single Crystal," *Micromechanics: Experimental Techniques*, W. N. Sharpe, Jr., Ed., ASME, NY, pp. 33-54, Dec.1989.
19. Dadkhah, M. and Kobayashi, A. S., "HRR Field of a Moving Crack, an Experimental Study," submitted to *Engineering Fracture Mechanics*.
20. Bowles, D. E., Post, D., Herakovitch, C. T. and Tenney, D. R., "Moire Interferometry for Thermal Expansion of Composites," *Experimental Mechanics*, vol. 21, no. 12, Dec. 1981.
21. Kang, B. S. -J, Wang, F. X. and Liu, Q. K., "High Temperature Moire Interferometry for Use to 550°C," *Proceedings of the 1990 fall Conference of the Society for Experimental Mechanics*, Baltimore, VA., Nov. 1990.
22. Czarnek, R., Post, D. and Herakovitch, C. T., "Edge effects in Composites by Moire Interferometry," *Experimental Techniques*, vol. 23(1), Jan. 1983.
23. Ifju, P. and Post, D., "Thermal Strain Analysis Using Moire Interferometry," *Proceedings of SPIE - The international Society for Optical Engineering*, vol. 814, Part 2, San Diego, California, Aug. 1987.
24. Kang, B. S. -J, Dadkhah, M. and Kobayashi, A. S., " J-Resistance Curves of Aluminum Specimens Using Moire Interferometry," *Proceedings of the 1989 Spring Conference of the Society for Experimental Mechanics*, Cambridge, MA., May 1989.

25. Post, D., Czarnek, R., Joh, D., Jo, J. and Guo, Y., "Experimental Study of a Metal-Matrix Composite," *Experimental Mechanics*, vol. 27, no. 2, pp. 190, June 1987.
26. Ruiz, C., Post, D. and Czarnek, R., "Moire Interferometric Study of Dovetail Joints," *J. Appl. Mech.*, 52, no. 1, pp. 109-114, Mar. 1985.
27. Epstein, J. S., Deason, V. A. and Abdallah, M. G., "Phenomenological Aspects of Bond Line and Mid-lamina Cracks in [0/90]<sub>s</sub> AS4/3501-6 Graphite/Epoxy Plates Under Stress Wave Loading," *Micromechanics: Experimental Techniques*, W. N. Sharpe, Jr., Ed., ASME, NY, pp. 55-71, Dec.1989.
28. Guo, Y., Post, D. and Czarnek, R., "The Magic of Carrier Patterns," *Experimental Mechanics*, vol. 29, no. 2, pp. 169-173, June 1989.
29. Post, D., "Analysis of Moire Fringe Multiplication Phenomena," *Applied Optics*, vol. 6, no. 11, pp. 1938-1942, Nov. 1967.
30. Post, D., "New Optical Methods of Moire Fringe Multiplication," *Experimental Mechanics*, 8(2), pp. 63-68, 1968.
31. Post, D., "Moire Fringe Multiplication with a Non-Symmetrical Doubly-blazed Reference Grating," *Applied Optics*, vol. 10, no. 4, pp.901-907, April 1971.
32. Sciammarella, C. A. and Lurowist, N., "Multiplication and Interpolation of Moire Fringe Orders by Purely Optical Techniques," *Journal of Applied Mechanics*, pp. 425-430, June 1967.
33. Post, D. and MacLaughlin, T. F., "Strain Analysis by Moire-fringe Multiplication," *Experimental Mechanics*, pp. 408-413, Sept. 1971.

34. Graham, S. M. and Sanford, R. J., "A Study of Residual Stress Effects on Fatigue Growth Using Moire," *Proceedings of the VI International Congress on Experimental Mechanics*, pp. 286-191, Portland Oregon, June 1988.
35. Morimoto, Y., Hayashi, T. and Wada, K., "High-Sensitivity Measurement of Strain by Moire Interferometry," *JSME, Series I*, vol. 32, no.1, 1989.
36. Czarnek, R., "Super High Sensitivity Moire Interferometry with Optical Multiplication," *Optics & Lasers in Engineering*, vol. 13, no. 2, pp. 87-98, 1990.
37. Hunter, A. R. and Martinson, R. L., "Fringe-Intensity Interpretation Method for High Sensitivity Moire Strain Analysis," *Proc. 1982 Joint SESA-JSME Conf. on Exp. Mech.*, SEM, pp. 52-57, 1982.
38. Hunter, A. R., Milly, T., Lopicz, D. and Bjeletich, J., "Application of Computerized Moire Technique to Study Fracture on Filament Wound Composites," *Proc. 1983 SESA Spring Conf. on Exp. Mech.*, SEM, pp.280-283, 1983.
39. Voloshin, A. S., Burger, C. P., Rowlands, R. E. and Richard, T. G., "Fractional Moire Strain Analysis Using Digital Image Techniques," *Experimental Mechanics*, vol. 26, pp.254-258, 1986.
40. Hung, Y. Y., Wang, N., Ruan, H. and Cheng, S. K., "Fringe Multiplication by Digital Image Processing," *Proc. Soc. Photo-Opt. Instrum. Eng.*, Vol 814, pp. 769-773, 1987.
41. Yu Q., "Fringe Multiplication Methods for Digital Interferometric Fringes," *Applied Optics*, vol. 28, no. 20, pp. 4323-4327, 1989.
42. Post, D., "Moire Interferometry," *Handbook on Experimental Mechanics*, A. S. Kobayashi, Ed., Prentice-Hall, Englewood Cliffs, NJ, 1987.

43. Weissman, E. M. and Post, D., "Moire Interferometry near the Theoretical Limit," *Applied Optics*, vol. 21, no. 9, May 1982.
44. Bonse, U., and Graeff, W., "X-Ray and Neutron Interferometry," *X-Ray Optics*, H.J. Queisser, Editor, Springer-Verlag, NY, 1977.
45. Dai, F., Mckelvie, J. and Post, D., "An Interpretation of Moire Interferometry from Wavefront Interference Theory," *Optics and Lasers in Engineering*, vol. 12, pp. 1-18, 1990.
46. Hecht, E. and Zajac, A. "Optics," Addison-Wesley Publishing Co., MA, 1979.
47. Post, D., "Moire Interferometry with White Light," *Applied Optics*, vol. 18, no. 24, pp. 4163-4167, 1979.
48. Durelli, A. J. and Riley, W. F., "Experimental Stress Analysis," 2nd ed., McGraw-Hill, NY, pp. 426-429, 1978.
49. Chiang, F. P., Parks, V. J. and Durelli, A. J., "Moire Fringe Interpolation and Multiplication," *Experimental Mechanics*, 8(12), pp. 554-560, 1968.
50. Chiang, F. P., "Moire Method of Strain Analysis," Chap.6, *Manual on Experimental Stress Analysis*, A. S. Kobayashi, Ed., Society for Experimental Stress Analysis, Bethel, CT. 1978.
51. Mckelvie, J., Pritty, D. and Walker, C. A., "An Automatic Fringe Analysis Interferometer for Rapid Moire Stress Analysis," *SPIE Proceedings*, vol. 164, Bellingham, WA, Sept. 1978.
52. Chang, M., Hu, C., Lam, P. and Wyant, C., "High Precision Deformation Measurement by Digital Phase Shifting Holographic Interferometry," *Applied Optics*, vol. 24, no. 22, pp. 3780-3783, Nov. 1985.

53. Hariharan, P., Oreb, B. F. and Brown, N., "A Digital Phase-measurement System for Real-time Holographic Interferometry," *Optics Communication*, vol. 41, no. 6, pp. 393-396, May 1982.
54. Patorski, K., "Moire Interferometry - Recent Developments" (to be published).
55. Shield, T. W. and Kim, K.-S., "Diffraction Theory of Optical Interference Moire and a Device for Production of Variable Virtual Reference Gratings: A Moire Microscope," submitted to *Experimental Mechanics*.
56. Wood, J. D., Tsai, M. Y., Post, D., Morton, J., Parks, V. J. and Gerstle Jr., F. P., "Thermal Strains in A Bimaterial Joint: Experimental and Numerical Analysis," *Proceedings of the 1989 Spring Conference of the Society for Experimental Mechanics*, Cambridge, MA., May 1989.
57. Post, D. and Wood, J. D., "Determination of Thermal Strain by Moire Interferometry," *Proceedings of the 1988 Fall Conference of the Society for Experimental Mechanics*, Indianapolis, Indiana, Sep. 1988.
58. Ifju, P. and Post, D., "Zero-thickness Specimen Gratings for Moire Interferometry," *Experimental Techniques*, vol. 15, no. 2, March/April 1991.

## Vita

Bongtae Han

Bongtae Han was born in Seoul, Korea on July 21, 1958 to Yoonchan and Enkyung Han. His college education began in 1977 when he was admitted to the engineering school of Seoul National University in Seoul, Korea. After completing his bachelor degree in the Mineral and Petroleum Engineering department in 1981, he pursued a master degree in the same department. He conducted research on the prediction of subsidence, under the direction of Prof. H. K. Lee. After receiving the M.S. degree in 1983, he was employed by Korea Industrial Research Institute in Seoul, Korea, where he conducted research on the methodology to evaluate government-funded projects before and after completion. Three years later, he went to Virginia Polytechnic Institute and State University to continue his graduate studies. In the winter of 1987, he began working in the photomechanics laboratory under the direction of Prof. Dan Post. Since then, he has conducted research on experimental solid mechanics. His current research interests comprise developments in moire interferometry, especially increasing its sensitivity, and micromechanical studies on grain and intergranular deformation of metals and ceramics, fiber/matrix interactions in fiber reinforced composite materials, and interface problems.

*Bongtae Han*